



**CHALMERS**  
UNIVERSITY OF TECHNOLOGY

## **Alkali emissions characterization in chemical looping combustion of wood, wood char, and straw fuels**

Downloaded from: <https://research.chalmers.se>, 2024-03-20 10:42 UTC

Citation for the original published paper (version of record):

Gogolev, I., Pikkarainen, T., Kauppinen, J. et al (2022). Alkali emissions characterization in chemical looping combustion of wood, wood char, and straw fuels. *Fuel Processing Technology*, 237. <http://dx.doi.org/10.1016/j.fuproc.2022.107447>

N.B. When citing this work, cite the original published paper.



# Alkali emissions characterization in chemical looping combustion of wood, wood char, and straw fuels

Ivan Gogolev<sup>a,\*</sup>, Toni Pikkarainen<sup>b</sup>, Juho Kauppinen<sup>b</sup>, Markus Hurskainen<sup>b</sup>, Anders Lyngfelt<sup>a</sup>

<sup>a</sup> Chalmers University of Technology, Sweden

<sup>b</sup> VTT Technical Research Centre of, Finland

## ARTICLE INFO

### Keywords:

Chemical looping combustion  
Alkali emissions  
Biomass conversion  
CO<sub>2</sub> capture  
Ash chemistry

## ABSTRACT

Chemical looping combustion of wood pellets (WP), wood char (WC), and straw pellets (SP) was conducted in a 60 kW CLC pilot with ilmenite and braunite oxygen carriers (OCs). Alkali emissions were investigated with impactor-based and surface ionization detector (SID) measurements. Particle size distributions for WP and WC fuels were dominated by coarse particles formed by refractory species. For SP fuel, the distribution was bimodal with a distinct fine particle mode formed by nucleation of volatile ash species. Thermodynamic modelling of stable alkali species at 800 °C predicted that high KOH(g) and lower concentrations of KCl(g) are stable for WP and WC fuels. For SP fuel, equilibrium K species were dominated by condensed-phase K species, followed by KCl(g), and KOH(g). Modelling of fuel-OC interactions showed that ilmenite decreases equilibrium levels of KOH(g) and KCl(g). Braunite impacted only KOH(g) levels. Impactor sample leachate analysis showed that for WP-braunite operation, the leachate contained KCl, NaCl, KOH, and NaOH, in decreasing order. For WC-ilmenite operation, the samples contained KOH and KCl. For SP fuel, most detected alkalis were KCl. For most cases, speciation of impactor samples qualitatively agreed with modelling predictions. Impactor and SID alkali measurements showed reasonable agreement for WC-braunite and SP-braunite tests.

## 1. Introduction

Chemical looping combustion of biomass (bio-CLC) is a promising bioenergy with carbon capture and storage (BECCS) technology. A simplified schematic of the CLC process is presented in Fig. 1. In CLC, an oxygen carrier (OC) material is circulated between two fluidized bed reactors. The OC is oxidized in the air reactor (AR) with air, and is then conveyed to the fuel reactor (FR), where the OC is reduced by fuel. In the case of solid fuels, such as biomass, the FR is fluidized with steam. The steam gasifies the biomass so that the gasification products can react with the OC material. The reduced OC then returns to the AR to be re-oxidized. In the CLC scheme, the OC is essentially used to separate oxygen from air and transport it to the fuel in the FR. The nitrogen from air is segregated to the AR flue gas. The resulting FR flue gas consists mostly of CO<sub>2</sub> and steam. Since steam is easily separated from CO<sub>2</sub> by condensation, the CLC scheme achieves fuel conversion with CO<sub>2</sub> capture in the FR flue gas. This inherent CO<sub>2</sub> separation is the major advantage of CLC technology, when compared to the costly and energy-intensive flue gas CO<sub>2</sub> separation that is required in post-combustion CO<sub>2</sub> capture. The details of the CLC operating principle have been

described in a number of publications [1–6]. Although CLC technology has seen several decades of development, early applications of CLC technology were focused on gaseous fuels, and later on solid fossil-derived fuels. CLC of biogenic solid biomass fuels is still in its infancy [7], with operation demonstrated in several experimental campaigns [8–14]. One of the biggest challenges for scale up and continuous operation of bio-CLC lies in understanding and controlling the issues that arise from the release of alkalis during conversion of biomass in a CLC system.

Since the bio-CLC process is based on fluidized bed technology, alkali related issues that are common to conventional fluidized bed biomass combustion and gasification processes may pose a major challenge to the implementation and scale-up of bio-CLC. In conventional fluidized bed biomass combustion and gasification, alkalis released to the gas phase are known to cause fouling and high-temperature corrosion of heat exchange surfaces [15–18]. Furthermore, alkalis that remain in the bed material are known to cause bed material agglomeration through formation of low melting point alkali silicate melts that act as a binder for the bed material [15,19].

The mechanisms of alkali release in conventional combustion and

\* Corresponding author at: Hörsalsvägen 7, SE-412 96 Gothenburg, Sweden.  
E-mail address: [gogolev@chalmers.se](mailto:gogolev@chalmers.se) (I. Gogolev).

<https://doi.org/10.1016/j.fuproc.2022.107447>

Received 20 May 2022; Received in revised form 14 July 2022; Accepted 30 July 2022

Available online 13 August 2022

0378-3820/© 2022 The Authors. Published by Elsevier B.V. This is an open access article under the CC BY license (<http://creativecommons.org/licenses/by/4.0/>).

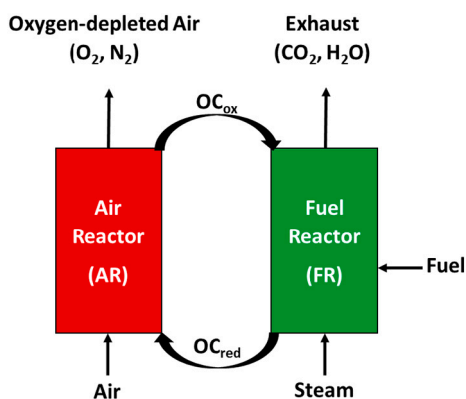


Fig. 1. Simplified schematic of the CLC process.

gasification processes have been studied over the past few decades, leading to strategies for mitigating alkali related issues. In the field of CLC, alkali release and the implications of alkali release are sparsely explored. To date, several studies have attempted to determine how alkali species are released and distributed in the two-reactor scheme of a CLC system [20–22]. In these investigations, a surface ionization detector (SID) was used to measure total gas-phase alkali emissions in the FR and the AR of several CLC pilot systems. While these SID-based measurements offered the first valuable insight into the extent and partitioning of alkalis in CLC pilot systems, the speciation of the alkalis released to the gas phase remained undetermined.

Determining the speciation of alkalis that are released in the CLC process is important in predicting the severity of corrosion and fouling that can result from their release. Of the different gaseous alkali species that are known to occur in thermochemical conversion of biomass, KCl (g) is considered to be especially corrosive to steel heat exchanger tubes.  $K_2CO_3(l,s)$ , which forms from a reaction  $KOH(g)$  and  $CO_2(g)$  as the flue gas cools in the convection pass, is considered to be moderately corrosive.  $K_2SO_4(g)$ , another common gaseous alkali, is known to be relatively benign from a corrosion point of view [18,23,24]. Thus, establishing the speciation of alkalis released to the gas phase of CLC units is an important research gap that has not yet been addressed in published literature. The aim of the current work was to provide the first insight into the speciation of the alkali emissions that occur in chemical looping combustion of biomass.

In the presented study, CLC operation of wood pellets (WP), wood char (WC), and straw pellets (SP) was conducted with ilmenite and braunite oxygen carrier (OC) materials in a 60 kW<sub>th</sub> CLC pilot system. Gaseous alkali emissions were measured with a SID-based system and with a Dekati low pressure impactor (DLPI) system. The SID technique provided online monitoring of total alkali emissions in the gas phase. The DLPI measurements determined fly ash concentration and particle size distribution. Chemical analysis of the particles captured by the DLPI was performed to establish alkali speciation in the flue gas. The DLPI technique was chosen since other studies have shown that alkalis that exist as vapors at flue gas conditions undergo condensation and nucleation into solid particles that are effectively captured by DLPI systems [25–27]. Further to experimental measurements, the study is augmented with thermodynamic modelling aimed at qualitatively differentiating the gaseous alkali speciation that can be attributed to the process of fuel conversion, and the effect that the OC materials have on the quantity and speciation of the released gaseous alkalis.

## 2. Background

The inorganic content of biomass fuels can vary significantly, from <1 wt% for woody biomass, up to 40 wt% in greenhouse residues. The most common of the inorganic species are Ca, K, Si, Mg, Al, S, Fe, P, Cl, Na, Mn, and Ti, listed in decreasing order of abundance [28]. The

inorganic matter found in biomass is responsible for ash formation.

### 2.1. Ash formation in biomass conversion

Ash forming species in biomass fuels can be grouped by their volatility. Elements like Ca, Si, Mg, Fe, and Al are known to be non-volatile. K, Na, S, Cl are known to be highly volatile, along with some heavy metals like Zn, Cd, and Pb [29,30]. Ash formed from biomass conversion is typically categorized as bottom ash or fly ash [17,18]. In fluidized bed systems, bottom ash is formed primarily from non-volatile species that are left over after char conversion [29,30]. Bottom ash particles are generally large, and depending on composition, can be sticky due to melt formation [18]. The majority of the bottom ash stays in the bed, where it either interacts with the bed material or remains as separate ash particles. Fly ash, the ash that is present in the flue gas, has two main origins that are typically grouped by particle size. Fine fly ash with a particle diameter < 1 μm is typically formed via condensation of volatile species that are released to the gas phase during fuel conversion. For biomass, the most relevant species are K, Cl and S, whereas Na and heavy metals typically have a minor contribution [18,29]. From these, gas-phase species particles initially form through nucleation of small primary particles that further grow through condensation, coagulation, and agglomeration. Coarse fly ash with a particle size > 1 μm arise from entrainment and stripping of smaller or fragmented bottom ash particles from the bed. These fly ash particles are primarily composed of the non-volatile species [17,18,29–31].

### 2.2. Alkali release and retention in biomass conversion

From the many inorganic species present in biomass fuels, K, Na, and Cl are considered highly problematic as their release is associated with fouling and corrosion of heat exchange equipment, and bed material agglomeration [15,23]. K and Na undergo the same release and transformation processes [18,32,33]. However, since K is present in great excess to Na in most biomass fuels, further discussion is focused on K. As biomass fuel is introduced into a reacting system (e.g., boiler, gasifier), it is heated and undergoes a staged decomposition process. As the fuel particle temperature rises, devolatilization starts to occur. This step is common to combustion and gasification processes. At the devolatilization stage, <10% of K is released at temperatures below 700 °C. Since the K release in the devolatilization step is quite small, most of the K species remain trapped in the char fraction as char-bound K, as K salts such as KCl,  $K_2CO_3$ , and  $K_2SO_4$ , and as K-silicates [34–38].

Further fuel decomposition differs for combustion and gasification. In combustion, char is oxidized to  $CO_2$ , while in gasification the char is gasified to CO and  $H_2$ . In both processes, the high temperature release occurs above 700 °C. For high alkali and chlorine content fuels the release is dominated by evaporation of KCl to the gas phase. The amount of KCl fraction in the char depends on the original fuel and on the amount of Cl that remains in the char after the devolatilization step. Several studies estimate that up to 75% of the fuel's Cl can be released at lower temperatures in the devolatilization stage through formation of HCl(g) [35,36,39]. Beyond KCl evaporation, further release of K occurs through devolatilization of char-bound K and decomposition of potassium salts, such as  $K_2CO_3$  and  $K_2SO_4$  [35,36,38,40,41]. Throughout the fuel conversion process, gas-phase release of K is counteracted by competing formation of K-silicates. At high temperatures K readily reacts with  $SiO_2$  and Al to form potassium silicate or aluminosilicate species. Silicate species remain in condensed form at temperatures below 1200 °C, but start to decompose releasing K to the gas phase at higher temperatures [35].

### 2.3. Implications of alkali release & retention

Alkali species released to the gas-phase are known to cause fouling and corrosion of heat exchange equipment in contact with the flue gases

[15,17,18,23,42]. In biomass fluidized bed boilers used for steam production, steam superheaters are operated at temperatures of approximately 400–600 °C, while typical combustion temperatures are maintained in the range of 800–900 °C [15,17]. Deposition of gaseous alkali species occurs as the flue gas begins to cool in the vicinity of the heat exchangers. Alkali salts condense onto the surface of the heat exchanger, forming a sticky coating. Further deposition occurs via further condensation of gaseous alkali species or by impaction of fly ash and other condensed species [15,17,23]. The deposits insulate the steam tubes and impede heat transfer, leading to lower overall heat extraction, and consequently lower boiler thermal efficiency.

Alkali species that remain in the bed material can also be problematic for boiler or gasifier operation. Alkali silicate species that form by reaction of alkalis with SiO<sub>2</sub> have a melting point of approximately 700 °C [15]. Since typical biomass-fueled furnaces operate at around 800–900 °C, alkali silicates form sticky melts. Once significant amounts of these melts are formed, the bed material particles start to stick together and form agglomerates. With continued operation, severe agglomeration of the bed material leads to defluidization and shutdown of the process units [15,17,23].

### 3. Material and methods

The experimental investigation presented herein is based on impactor measurements of FR and AR flue gas alkali emissions collected during CLC operation of a dual circulating fluidized bed (D-CFB) process development unit (PDU) located at VTT Bioruukki piloting center in Espoo, Finland. A schematic of this pilot system is presented in Fig. 2.

The D-CFB unit consists of two interconnected circulating fluidized beds (CFB). Each CFB consists of a high velocity riser, a cyclone, and a return leg that interconnects the CFBs. In CLC operation, one of the unit's CFBs was used as the AR and was fluidized with air. The second CFB was used as the FR and was fluidized with steam. Biomass fuel was fed from a fuel hopper to the FR with a screw feeder. Fig. 2 points out the alkali sampling locations used for the impactor and SID-based alkali measurements. The impactor-based alkali emissions measurement campaign

was conducted concurrently with a SID-based alkali emissions measurement campaign. Detailed analysis of the SID-based alkali measurements has been published by Gogolev et al. [22]. The impactor-based alkali emissions results are presented and analyzed in the present work. SID-based measurements that were collected concurrently with the impactor sampling periods are included in the present work to facilitate comparison of the two alkali measurement methodologies. A detailed description of the pilot system and the SID-based alkali measurement setup can be found in Reference [22].

#### 3.1. Test campaign, fuels and oxygen carriers

The test campaign included seven CLC tests that were performed over three days of operation. On the first day of the campaign the pilot was operated with ilmenite OC, and WP and WC fuels. On the second and third days of the campaign the pilot was operated with braunite OC, and WP, WC, and SP fuels. WP and SP fuels were used in the form of crushed pellets. WC fuel was used in the form of coarse char particles. A summary of the CLC tests is presented in Table 1.

Detailed information on the CLC campaign can be found in Reference [22]. Fuel properties and composition are presented in Table 2. OC composition is presented in Table 3.

**Table 1**  
CLC operation summary.

Operation day	CLC test	Oxygen carrier	Fuel	Fuel feed rate (g/s)	Test duration (hh:mm)
Day 1	1	Ilmenite	WP	1.9	01:13
	2*		WP	2.5	00:39
	3		WC	2.4	01:25
	4		WC	3.3	00:39
Day 2	5	braunite	WP	3.7	02:51
	6		WC	2.8	00:56
Day 3	7		SP	3.0	01:58

\* Note: CLC operation with fuel fed into the FR and AR.

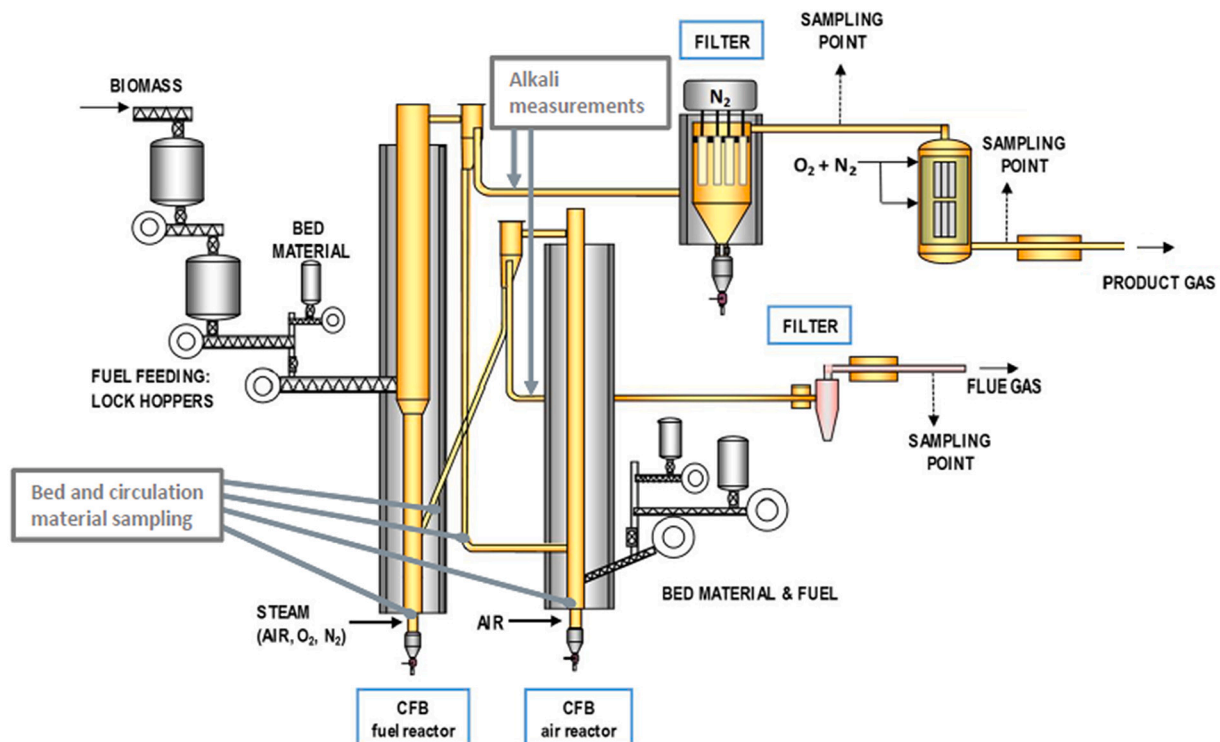


Fig. 2. Schematic of the dual circulating fluidized bed chemical looping combustion pilot. Reprinted from Reference [22], with permission from Elsevier.

**Table 2**  
Fuel properties and composition.

Parameter	Unit	WP	WC	SP
Moisture	wt% a.r.	7.50	4.10	8.10
Ash	wt% a.r.	0.460	14.0	5.51
Volatiles	wt% a.r.	78.4	18.7	69.3
Fixed Carbon	wt% a.r.	13.7	63.2	17.1
H	wt% a.r.	5.64	2.21	5.24
C	wt% a.r.	46.9	73.0	43.2
N	wt% a.r.	0.160	0.960	0.580
O	wt% a.r.	39.4	5.75	37.2
K	mg/kg fuel a.r.	403	3115	13,732
Na	mg/kg fuel a.r.	244	229	123
Cl	mg/kg fuel a.r.	26.0	101	3320
S	mg/kg fuel a.r.	93.0	288	1010
Si	mg/kg fuel a.r.	88.0	378	9210
Ca	mg/kg fuel a.r.	994	47,000	3360
LHV	MJ/kg a.r.	17.3	26.1	15.8
Bulk Density	kg/m <sup>3</sup> a.r.	476	368	332
Particle Size Range	mm	2–6	3–8	2–6

**Table 3**  
Oxygen carrier composition.

Element	Unit	Ilmenite	Braunite
Ti	wt%	27.36	0.020
P	wt%	0.004	0.030
S	wt%	0.026	0.13
Cr	wt%	0.051	0.010
Fe	wt%	35.89	11.0
Si	wt%	0.76	2.50
V	wt%	0.11	<0.01
Ca	wt%	0.15	3.50
Mg	wt%	2.23	0.89
Al	wt%	0.34	0.25
Mn	wt%	0.23	55.0
K	wt%	0.017	0.020
Na	wt%	0.052	0.22
Zn	wt%	0.012	0.010
Ni	wt%	0.018	0.010
Cu	wt%	0.007	0.040
Co	wt%	0.012	0.020
Sr	wt%	0.003	0.12
Zr	wt%	0.017	0.020
Nb	wt%	0.005	<0.0001
Pb	wt%	<0.0001	0.010
Cl	wt%	<0.01	0.030
O (remainder)	wt%	32.7	26.2

### 3.2. Impactor-based alkali measurement system

Alkali emissions resulting from CLC operation were measured with two independent measurement systems. The SID-based alkali measurement system was used for online measurement of gaseous alkali emissions. The overview of the SID-based measurement system, as well as detailed SID measurement results are available in Reference [22]. In parallel with the SID measurements, alkalis were also sampled with an impactor-based alkali measurement system. A schematic of the impactor-based alkali measurement system is presented in Fig. 3.

The impactor-based alkali measurement system samples the flue gas via a specially designed probe. The probe was installed in the flue gas chimney downstream of the FR cyclone in CLC tests 2, 3, 5, 6, and 7, and switched to the flue gas chimney downstream of the AR cyclone in the second part of CLC test 7. During sampling, the probe samples the gas at full process temperature (750–850 °C). The probe is air-cooled and is maintained at temperature of 180 °C. As the flue gas enters the probe, it is cooled and diluted with nitrogen in a wall-flow diluter that is integrated into the probe tip. The dilution nitrogen is supplied and controlled by the Environics S-2000 gas blender. The dilution nitrogen is doped with SF<sub>6</sub> gas that is used to confirm the probe's dilution ratio. The diluted sample leaving the probe is split into two streams. One of the

streams flows through a filter to remove solid particles, and then splits into two flows. One flow follows to a Fourier transform infrared (FTIR) gas analyzer (Gaset DX-4000) via a pump unit, and the other to a CO<sub>2</sub>/CO/O<sub>2</sub> gas analyzer. The FTIR reports concentrations for various hydrocarbon species, as well as for HCl, SO<sub>2</sub>, SF<sub>6</sub>, and water. The sample lines from the probe to the FTIR and gas analyzers, as well as the filter, are electrically heated and maintained at 180 °C.

The second stream after the sampling probe is drawn by a Dekati® ejector diluter. This diluter creates the sample suction and facilitates secondary dilution of the sample with more nitrogen. The sample flow after the secondary dilution is split between an electrical low pressure impactor (ELPI) and two parallel Dekati® low pressure impactors (DLPI). The flow to the ELPI is routed via a PM10 cyclone and another Dekati® ejector diluter. The cyclone rejects solids particles larger than 10 µm, while the ejector diluter facilitates tertiary dilution of the sample before it enters the ELPI. The ELPI was used to measure the particle count concentration and mass size distribution of the sample flow. The flows to the two DLPI units are routed via PM10 cyclones. Each of the parallel DLPI units contain 13 impactor stages corresponding to 13 particle size ranges, arranged in decreasing order. Each of the stages contains a greased polycarbonate foil that captures particles that are too large to pass on to the next impactor stage.

For each measurement period, each of the two DLPI units is loaded with new foils, with every foil carefully weighed before installation. The system then samples the flue gas for a duration of 20–70 min, depending on the test. After sampling is complete, the DLPI units are disassembled, and the foils are carefully weighted to determine the amount of sample trapped at each impactor stage to produce a particle mass size distribution. The samples from the 13 impactor stages are then grouped into four size ranges (<0.03, 0.03–0.16, 0.16–0.6, 0.6–2.4, 2.4–10 µm). The material contained on the foils within each size range are then leached and analyzed. Samples from one impactor were leached in water and analyzed by inductively coupled plasma mass spectrometry (ICP-MS) for cation concentration and with ion chromatography (IC) for anion concentration.

Once the sample mass and elemental composition are established, the concentration of each of the species identified in the analyses can be calculated by dividing the mass by the volume of diluted sample flow that passed through the DLPI units over the sampling period, and multiplying the result by the overall dilution factor of the DLPI unit. The sample volume can be determined from the sample time and flow rate of the DLPI vacuum pump. The overall dilution ratio of the DLPI sample is calculated as product of the primary and secondary dilution ratios. The primary dilution ratio is calculated by dividing the CO<sub>2</sub> concentration of the flue gas (reported by the main process analyzers – not shown in Fig. 3) by the CO<sub>2</sub> concentration of the sample after the first dilution stage (reported by the CO<sub>2</sub>/CO/O<sub>2</sub> analyzer, shown in Fig. 3). Additionally, the primary dilution ratio is also double checked with a balance of SF<sub>6</sub> gas concentration which is measured by the FTIR analyzer. The secondary dilution ratio is fixed to a value of 2.8 x by the Dekati® ejector diluter. Further to correction for dilution, the species concentrations from the analysis of DLPI samples are also corrected to dry conditions, using the moisture content measurement reported by the FTIR. For particle count measurements, ELPI results are also corrected for dilution and moisture. The only difference is that the ELPI sample is diluted in three stages, instead of two. The first two dilution stages are the same as for the DLPI unit, and the third stage of dilution is fixed at 11x by the Dekati® ejector diluter at the inlet of the ELPI analyzer.

### 3.3. Thermodynamic modelling

In order to support the interpretation of the chemical analysis of DLPI samples, global equilibrium of CLC fuel conversion was modelled in FactSage 7.2 software. This thermodynamic modelling software is based on Gibbs free energy minimization in a mass balance constrained system. The model assumes ideal mixing and is not constrained by mass



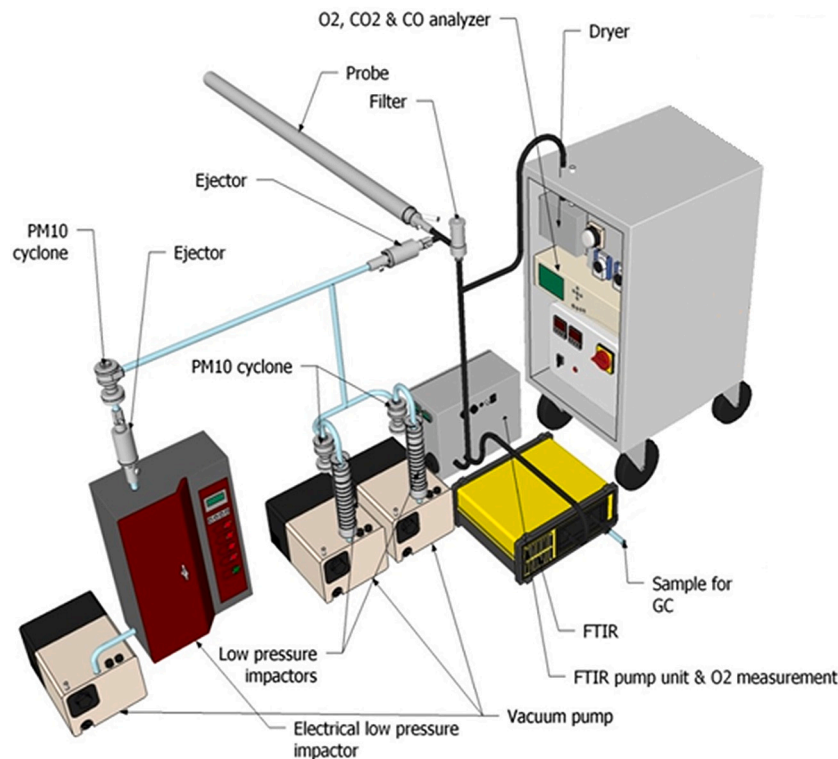


Fig. 3. Impactor-based alkali measurement system.

transport or chemical reaction kinetics. The lack of transport and chemical kinetic limitations, and the assumption of perfect elemental mixing are highly unlikely since biomass is a highly heterogeneous and multi-phase fuel. However, thermodynamic predictions can still provide valuable information on what type of alkali species are able to form [43]. For each biomass fuel used in the experiments, two thermodynamic models were created: 1) a model of fuel conversion without influence of the oxygen carrier, and 2) a model of fuel conversion in equilibrium with the oxygen carrier. The databases and species were included in the FactSage model are summarized in Table 4.

### 3.3.1. Model of fuel conversion without OC influence (Fuel+O<sub>2</sub> Model)

Equilibrium products of fuel conversion were first considered without the influence of the oxygen carrier. The elemental composition of the fuel was input into FactSage along with nitrogen, steam, and oxygen. The amounts of nitrogen and steam were based on the amount of nitrogen and steam that were injected into the FR during the CLC experiments. Oxygen was added to the model to simulate oxygen sourced from an oxygen carrier. The amount of oxygen added in the simulation was based on the proportion of stoichiometric oxygen that reacted with the fuel during the CLC experiments. A well-established parameter in the field of CLC research is the oxygen demand,  $\Omega_{OD}$ . The oxygen demand is defined as the ratio of the oxygen required to fully oxidize the flue gas of the fuel reactor to the stoichiometric oxygen

required for complete fuel oxidation. Oxygen demand is calculated as:

$$\Omega_{OD}[\%] = 100 \times \frac{0.5X_{CO,FR(dry)} + 2X_{CH_4,FR(dry)} + 0.5X_{H_2,FR(dry)}}{\Phi_o (X_{CO_2,FR(dry)} + X_{CO,FR(dry)} + X_{CH_4,FR(dry)})} \quad (1)$$

Here  $\Phi_o$  is the O<sub>2</sub>/C molar ratio [mol O<sub>2</sub> required for combustion/kg fuel] / [mol C/kg fuel]. The proportion of stoichiometric oxygen that reacted with the fuel, commonly referred to as gas conversion efficiency  $\eta_{g.c.}$ , can then be calculated from the oxygen demand:

$$\eta_{g.c.}[\%] = 100\% - \Omega_{OD}[\%] \quad (2)$$

Gas conversion efficiency of the conducted CLC experiments ranged from 30 to 70%, meaning that 30 to 70% of the stoichiometric oxygen reacted with the fuel. In order to simplify the comparison of modelling results, all three biomass fuels were modelled with an addition of oxygen that is equivalent to 50% of the stoichiometric oxygen amount. After entering the fuel, N<sub>2</sub>, steam, and O<sub>2</sub> data, the FactSage simulations were carried out at 20 °C temperature steps in the range of 400–1000 °C. From the predicted species, species accounting for >1% of fuel K were plotted vs. temperature. The resulting plots are presented and discussed in Section 4.2.1.

### 3.3.2. Model of fuel conversion in equilibrium with the OC (Fuel+OC Model)

To simulate the effect of the OC on fuel conversion, a second FactSage model was developed for each fuel-OC pair. First, the oxidation of the OC was simulated at AR conditions (excess air, 800 °C). The resulting composition of the oxidized OC was combined with the fuel composition, along with nitrogen and steam. A simulation of OC reaction with the fuel was then carried out at 800 °C (average FR temperature). To show the effect of the OC, the model was run with a stepwise increase of the OC to fuel mass ratio,  $R_{OC/F}$ . From the calculated equilibrium results, K species that account for >1% of fuel K were plotted vs.  $R_{OC/F}$  parameter. The  $\eta_{g.c.}$ , calculated from the equilibrium concentrations of CO, CO<sub>2</sub>, H<sub>2</sub>, and CH<sub>4</sub>, was also included in the plots. The resulting plots are presented and discussed in Section 4.2.2.

Table 4  
Databases, species, and phases included in the FactSage models.

Database	Species/phases included
FactPS	Pure stoichiometric gas and solid phases
FToxid	Slag A: liquid oxide melt MeO: monoxide rock salt structure solution
FTSalt	CSOB: [Li], Na, K//SO <sub>4</sub> ,CO <sub>3</sub> (ss) low lithium content solid solution KCOH: KCl-KOH(ss) high temperature solid binary solution LCSO: liq-K, Ca//CO <sub>3</sub> ,SO <sub>4</sub> SCSO: K <sub>2</sub> [Ca]//CO <sub>3</sub> ,SO <sub>4</sub> (ss) solid solution

Lastly, the OC and fuel equilibrium model was also run to simulate the conditions experienced during the five FR impactor sampling periods, DLPI 1 to DLPI 5. For these cases, the FR temperature, steam, and nitrogen amounts are summarized in Table 5 (see Section 4.1). The amount of OC in equilibrium with the fuel was iteratively determined, matching a condition where the  $\eta_{g.c.}$  value calculated from the model's equilibrium predictions matched the average experimental  $\eta_{g.c.}$  value for the individual impactor sampling periods. The model predictions for the impactor sampling periods are presented and discussed in Section 4.2.3.

## 4. Results and discussion

The results of the study are summarized and discussed in the following subsections.

### 4.1. Flue gas particle concentration and size distribution

A summary of the operating conditions and DLPI sampling results for CLC operation with WP, WC, and SP fuels with ilmenite and braunite oxygen carriers is presented in Table 5. The average gas conversion efficiency,  $\eta_{g.c.}$ , of the CLC operation within the span of each DLPI measurement period is also included for reference in further discussion.

Results presented in Table 5 show that the particle mass concentrations collected by the DLPI system were in the range of 260–1800 mg/ $\text{Nm}^3_{\text{dry}}$ . This is in line with values reported for fluidized bed combustion of biomass [30,44]. However, it should be noted that the DLPI sampling was not isokinetic. Thus, the reported values likely underreport true flue gas particle concentrations. The particle mass concentration increases for operation WP, SP, and WC, respectively. Thus, higher particle mass concentrations occur for fuels of higher ash content. This behavior is consistent with the particle mass concentration dependence on fuel ash content in conventional biomass fluidized bed combustion [30]. In the presented tests results, the effect of the oxygen carrier is unclear. For operation with WP fuel, higher particle mass emissions are measured for operation with ilmenite. The opposite is true for operation with WC fuel, where particle mass emissions for operation with braunite are higher than for operation with ilmenite OC. Particle mass size distributions for all tests are presented in Fig. 4.

In Fig. 4, particle size distribution for WP fuel operation with braunite (Fig. 4b) and WC fuel operation with ilmenite and braunite (Fig. 4c and d) are dominated by coarse mode particles (particles  $>1 \mu\text{m}$ ), suggesting that most of the fly ash is composed of non-volatile ash species that originate from entrainment of smaller or fragmented ash particles. For WP fuel operation with ilmenite (Fig. 4a), and SP fuel operation with braunite (Fig. 4e and f) the particle size distribution appears to be bimodal. The bimodal distribution shape is more typical for fluidized bed biomass combustion where fine mode particles are formed through condensation of volatile inorganic species and the coarse mode particles originate mostly from elutriated ash formed from non-volatile species [29,30]. The high proportion of fine mode particulate in Fig. 4e and f suggests that the alkali content of the fly ash in operation with SP fuel can be quite high.

**Table 5**  
DLPI results and key process parameters.

DLPI Sample	CLC Test	Fuel	OC	Reactor Sampled	Reactor Bed Temp (°C)	Steam Addition to FR (mol H <sub>2</sub> O/kg fuel)	Nitrogen Addition to FR (mol N <sub>2</sub> /kg fuel)	Gas Conversion Efficiency $\eta_{g.c.}$ (%)	DLPI Sampling Time	DLPI Sample Mass (mg)	Particle Mass Conc. (mg/ $\text{Nm}^3_{\text{dry}}$ )
DLPI 1	2	WP	Ilmenite	FR	800	209	34	49.1	00:30	2.42	437
DLPI 2	3	WC	Ilmenite	FR	793	185	32	33.5	01:02	14.0	625
DLPI 3	5	WP	Braunite	FR	828	142	29	70.2	00:53	5.07	261
DLPI 4	6	WC	Braunite	FR	816	150	30	57.6	00:40	28.6	1806
DLPI 5	7	SP	Braunite	FR	817	109	28	64.4	00:20	3.03	837
DLPI 6	7	SP	Braunite	AR	857	109	28	63.3	00:20	2.30	381

### 4.2. Thermodynamic modelling results

In order to help in interpreting alkali speciation from analysis of the DLPI sample leachate (discussed in Section 4.3), thermodynamic modelling was used to establish what alkali species are likely to form in the CLC process. Fuel conversion for the WP, WC, and SP fuels was modelled in FactSage 7.2, as per the methodology described in Section 3.3. The following subsections discuss the results of thermodynamic modelling.

#### 4.2.1. Alkali release from fuel in absence of the OC

FactSage modelling results for fuel conversion at CLC conditions without the influence of OC are shown in Figs. 5 to 7 for the three fuels used in the experiments. In the model, each fuel is in equilibrium with nitrogen, steam, and oxygen. Nitrogen and steam amounts are representative of the experimental conditions in the pilot system. Pure oxygen is used in this model as a surrogate for the oxygen supplied by the OC. Since pure oxygen is used, this model represents a hypothetical case that demonstrates alkali speciation tendencies without the presence of the OC. Oxygen is provided at 50% of the stoichiometric amount, corresponding to the approximate level of gas conversion achieved in the pilot experiments. Table 6 provides a summary of the nitrogen, steam, and oxygen amounts used for each of the fuels in the model.

The model results in Figs. 5 to 7 show thermodynamically stable K species vs temperature. Since the K content of the three biomass fuels far exceeds that of Na, modelling of K species was prioritized. The associations shown for K species are assumed to also apply to Na species, since K and Na chemical behavior is known to be quite similar [18,32,33]. It is important to emphasize that this model does not attempt to represent the actual alkali release process that occurs during fuel conversion, but rather indicates the likely stable alkali species that would form in perfect equilibrium (perfect elemental mixing, no kinetic limitations). The intent of these models is to determine the speciation of the gaseous alkali species that can be expected in the flue gas of the fuel reactor.

Figs. 5 to 7 show that for all three fuels, gaseous K species become thermodynamically stable at temperatures above 500 °C. Below 500 °C, the predicted stable condensed-phase species are K-Ca-carbonates ( $\text{K}_2\text{Ca}_2(\text{CO}_3)_3$  and  $\text{K}_2\text{Ca}(\text{CO}_3)_2$ ),  $\text{K}_2\text{CO}_3$ , and KCl for all three fuels. Additionally,  $\text{K}_2\text{Si}_2\text{O}_5$  is predicted for the SP fuel. These predicted stable species should not be confused with the actual species present in the virgin fuel. K is known to be present in biomass in three main forms: organically associated, salts, and excluded minerals. The organically associated and salt forms are known to be releasable during thermal fuel conversion [18]. Alkali salts can account for up to 90% of alkalis in woody and herbaceous biomass [35,45,46]. The most common alkali salts found in biomass are phosphates, carbonates, sulphates, chlorides, and nitrates [28,47–49]. As such, KCl and  $\text{K}_2\text{CO}_3$  predicted by thermodynamic equilibrium make sense, and are likely forms of K to be contained in the actual fuels. The K-Ca-carbonates, on the other hand, are not known to be originally present in biomass fuels. These species are rather products of secondary reactions that occur during the fuel decomposition process. K-Ca-carbonates have been found in ashes of gasified and combusted biomass fuels [32,43]. Thus, K that is included in the predicted K-Ca-carbonates exists in a different form in the virgin

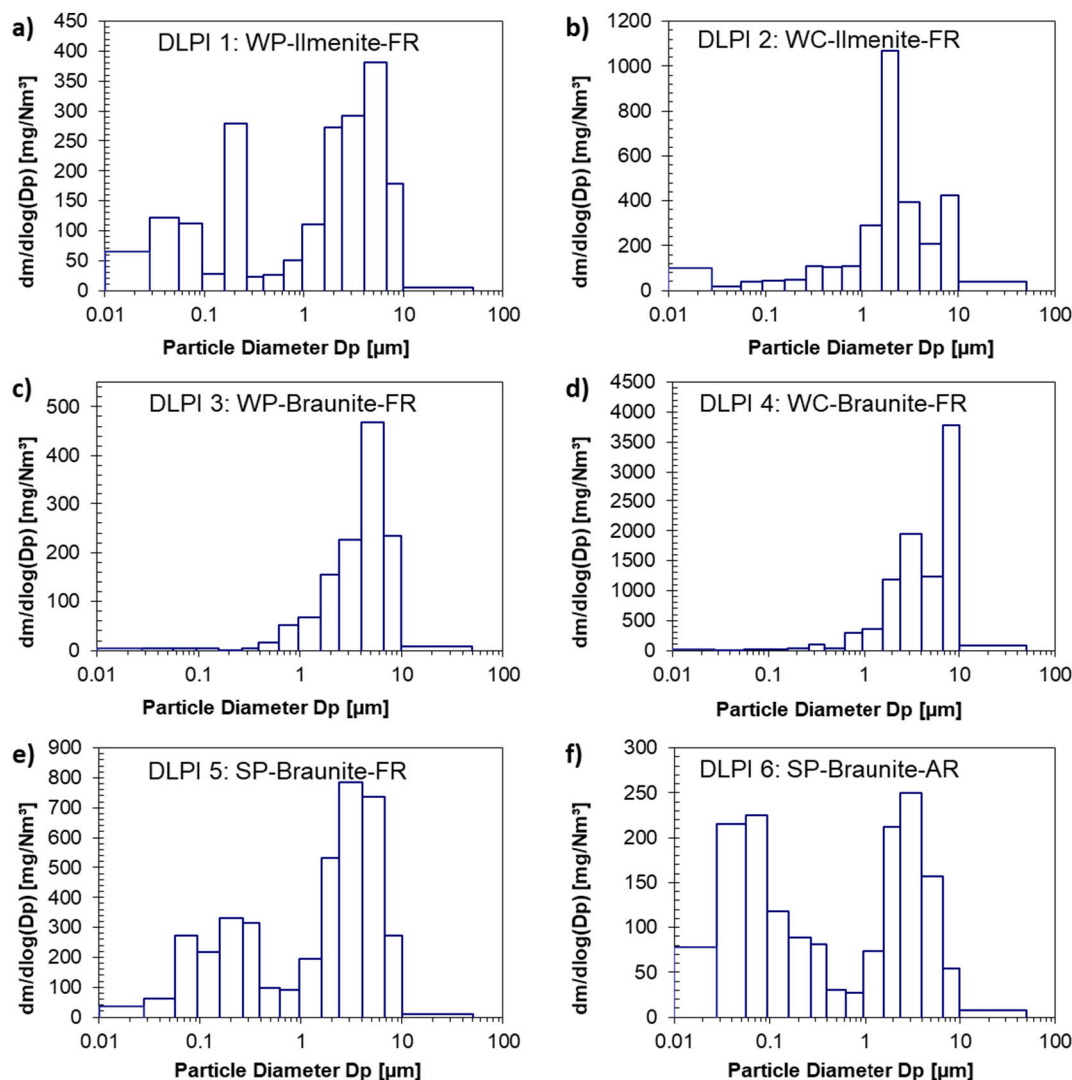


**Fig. 4.** Particle mass size distributions for a) wood pellets and ilmenite CLC – FR fly ash, b) wood char and ilmenite CLC – FR fly ash, c) wood pellets and braunite CLC – FR fly ash, d) wood char and braunite CLC – FR fly ash, e) straw pellets and braunite CLC – FR fly ash, f) straw pellets and braunite CLC – AR fly ash.

fuel, most likely as one of the salts mentioned above. The K-silicates predicted for SP fuel are also not a likely form for alkalis in the virgin fuel. Most of the Si content in agricultural residues occurs due to fuel contamination with  $\text{SiO}_2$  during the harvesting process. This form is known to be relatively unreactive in thermal fuel conversion [18]. For straw fuels, such as the SP fuel used in this study, up to 25% percent of the Si can be present in the organic matrix of straw fuels. This form of Si is reactive and can form K-silicates [18]. However, K-silicate formation is only relevant at higher temperatures. Below 700–800 °C alkali silicate formation is known to be kinetically limited [36]. Thus, the K predicted by the model to be associated as K-silicate below 700 °C, likely exists in the organic fraction of the fuel, or as a salt.

In Figs. 5–7, gaseous alkalis begin to be thermodynamically stable at temperatures above 500 °C.  $\text{KCl(g)}$  stability grows with temperature above 500–600 °C. At the same time,  $\text{KCl(s)}$  stability decays. As mentioned above,  $\text{KCl(s)}$  is a known form of alkalis in biomass fuels. In fuel conversion, this form is known to be released to the gas phase through sublimation of  $\text{KCl(s)}$  to  $\text{KCl(g)}$  at temperatures approaching 700 °C. The occurrence of  $\text{KCl(g)}$  in thermal biomass conversion has been confirmed by direct gas-phase observations [26,50,51].  $\text{KCl}$  sublimation is known to occur at pyrolysis, gasification, and combustion conditions, and is thus relevant at reducing, oxidizing, and steam-rich reducing conditions [35,36,40,52]. Thus, the model results in Figs. 5–7

seem to capture the extent and the temperature dependence of the  $\text{KCl}$  sublimation process. Beyond 650–700 °C,  $\text{KOH(g)}$  is predicted to become stable with increasing temperature. Increasing stability of  $\text{KOH(g)}$  with temperature is mirrored by a decay in stability of  $\text{K}_2\text{CO}_3$  and K-Ca-Carbonates. Release of  $\text{KOH(g)}$  to the gas phase during biomass combustion and gasification has been directly observed by molecular beam mass spectrometry [50,51].  $\text{KOH(g)}$  is thought to arise from a reaction of  $\text{K}_2\text{CO}_3$  with steam [35,52–54] or a reaction of steam with char-bound K at temperatures above 700–800 °C [35]. Thus, the model results in Figs. 5–7 seem to reflect the dependency of  $\text{KOH(g)}$  release vs. temperature. One surprising result is that  $\text{KOH(g)}$  accounts for >90% of the fuel K at temperatures above 900 °C for the WP and WC fuels. Furthermore, no condensed K species are predicted above 900 °C for WP and WC fuel. This prediction is not realistic since multiple investigations of alkali release report that the total K release in combustion and gasification of biomass is typically below 50% for temperatures of up to 1000 °C [36,43,52,55]. However, close to full release of K has been reported for Si-lean biomass at temperatures exceeding 1000 °C [35]. The full K release predicted by the model is likely a result of the assumptions of perfect elemental mixing and no kinetic limitations that is inherent in the model. Full release of K to the gas phase has been reported in thermodynamic modelling performed by other researchers, but was shown to be a result of the oversimplifying model assumptions [52,56]. It is also



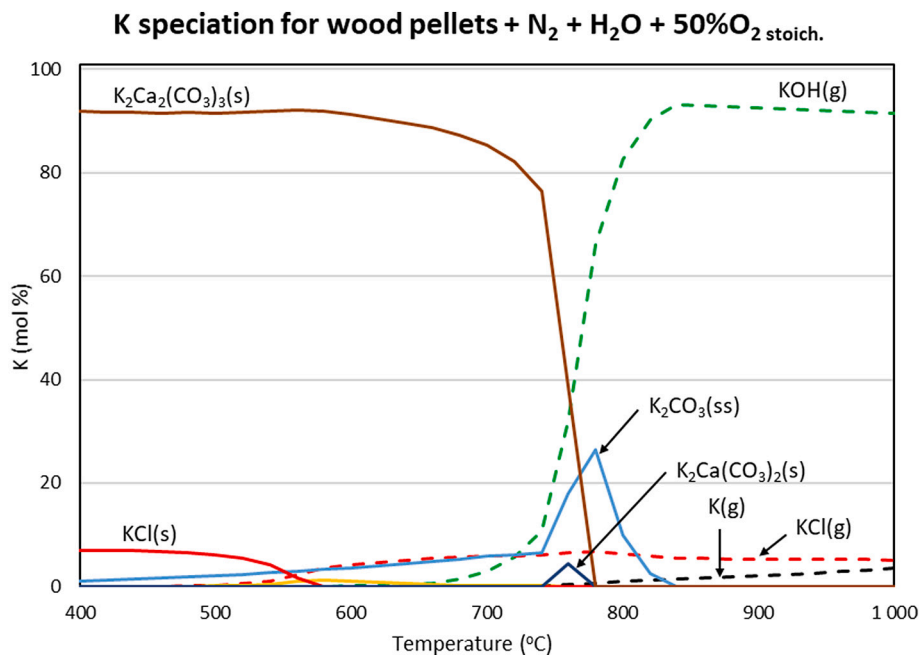


Fig. 5. Equilibrium K-species for reaction of wood pellets fuel with nitrogen, steam, and oxygen.

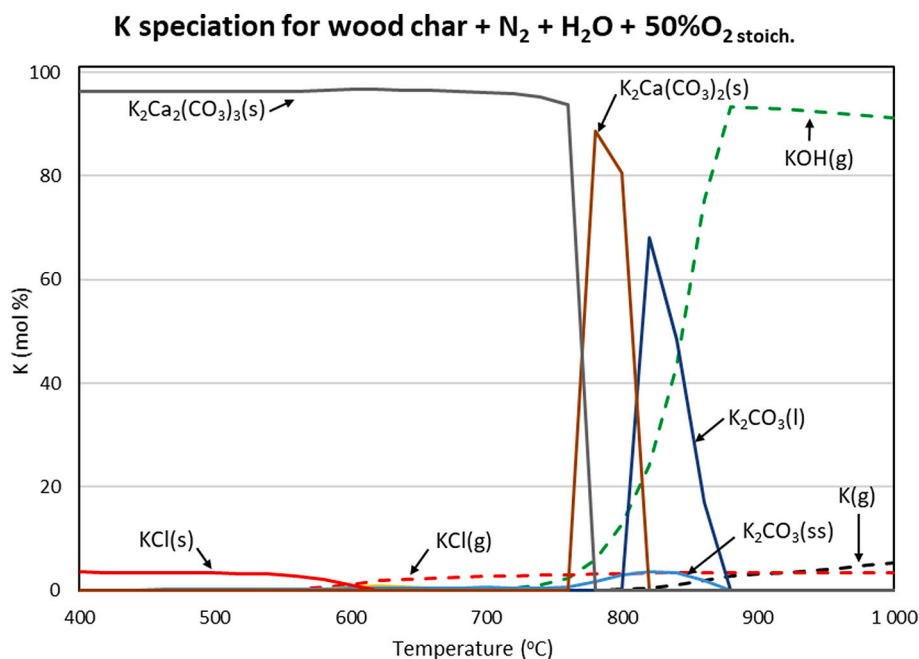


Fig. 6. Equilibrium K-species for reaction of wood char fuel with nitrogen, steam, and oxygen.

possible that the FactSage is missing some of the thermodynamic data for species that can retain K in condensed phases at temperature above 800 °C. For the SP fuel, which is a silica-rich fuel, the gas-phase release of alkalis is predicted to be below 40% in the 800–1000 °C temperature range. Gaseous release is predicted to be limited by capture of K in K<sub>2</sub>O slag and K<sub>2</sub>Si<sub>2</sub>O<sub>5</sub> condensed species. This prediction is qualitatively consistent with experimental observations of K release in combustion of straw [57,58]. Aside from KCl and KOH, the FactSage model predicts that K(g) can be stable above 800 °C for WP and WC fuels. Release of K(g) is known to be possible in strongly reducing conditions [18], such as the conditions in CLC operation. For SP fuel, (KCl)<sub>2</sub>(g) is predicted above 650 °C, but the stability of this specie decays beyond 750 °C with a clear

transition to KCl(g).

Another notable observation from the modelling results in Figs. 5–7, is that K does not seem to be associated with sulfur (S) for any of the fuels. K<sub>2</sub>SO<sub>4</sub> is a common form of K in virgin biomass as well as biomass gasification and combustion ash [32,35,43]. In combustion and gasification, K<sub>2</sub>SO<sub>4</sub> can contribute to the gaseous K release through evaporation which occurs above 1000 °C [35,36,51,56]. The FactSage model used to generate the K species distribution in Figs. 5–7 predicts that S is present primarily as H<sub>2</sub>S(g) at the CLC experimental conditions. Adjusting the amount of oxygen in the model reveals that at the experimental conditions experienced in the CLC pilot unit, K<sub>2</sub>SO<sub>4</sub> is not predicted to be stable. Fig. 8 shows the modelled effect oxygen

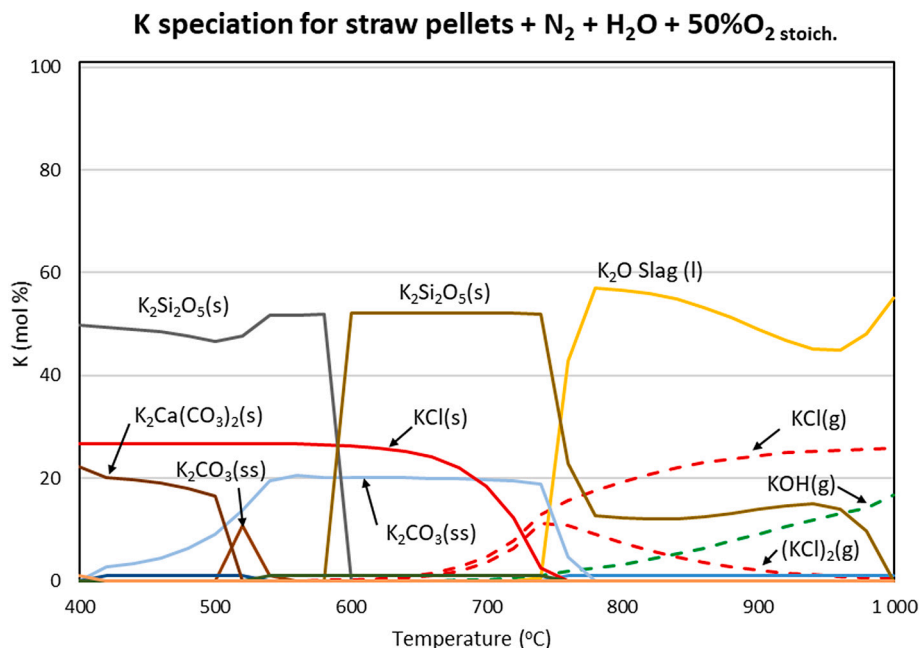


Fig. 7. Equilibrium K-species for reaction of straw pellets fuel with nitrogen, steam, and oxygen.

Table 6

Steam, nitrogen, and oxygen amounts used in the model.

Fuel	Steam (mol/kg fuel)	N <sub>2</sub> (mol/kg fuel)	O <sub>2</sub> (mol/kg fuel)
WP	176	31	20
WC	201	35	32
SP	152	38	19

availability on the stability on alkali sulfates,  $K_2SO_4$  and  $Na_2SO_4$ . Oxygen availability in Fig. 8 represents the ratio of the oxygen in equilibrium with the fuel to the stoichiometric amount of oxygen required for full fuel conversion. S species concentrations are expressed in terms of mol percentage of total S in the fuel. The oxygen availability range experienced in the pilot experiments is indicated for each fuel. This range was determined from the average  $\eta_{g.c.}$  values of the experiments.

Fig. 8 shows that in the experimental operating range, close to 100% of the fuel S is predicted to be stable as  $H_2S(g)$ . Alkali sulfates,  $K_2SO_4$  and  $Na_2SO_4$ , are predicted to be thermodynamically stable only above 85% of stoichiometric oxygen availability for WP and SP fuels and in excess oxygen conditions for the WC fuel. Fig. 8 indicates that the experimental conditions of the CLC experiments in this study are too reducing for alkali sulfate stability. This suggests that any  $K_2SO_4$  that may be present in the virgin fuels would dissociate to form  $H_2S$ , while K will be incorporated into a non-sulfate species.

In summary, thermodynamic modelling of fuel decomposition at CLC conditions, but with exclusion of the effect of the oxygen carrier, suggests the following key tendencies of gaseous alkali release behavior:

- The major gaseous alkali species are  $KCl(g)$ , which is released at temperatures above 500–600 °C, and  $KOH(g)$ , which is released above 650–750 °C
- At the experimental temperatures of 800 °C,  $KOH(g)$  release dominates  $KCl(g)$  release in WP and WC fuels, while  $KCl(g)$  and  $(KCl)_2(g)$  release dominates for the SP fuel
- Minor release of  $K(g)$  may be possible at 800 °C for WP and WC fuels
- $K_2SO_4(g)$  is not expected to be present in the gaseous phase for any of the fuels

#### 4.2.2. Alkali release from fuel in equilibrium with the OC

The trends described in Section 4.2.1 represent an idealized case of the fuel's natural tendency to form various K species upon high temperature oxidation. In the actual CLC process, these trends are expected to be influenced by interaction of fuel with the OC material. To identify the effect of the OC, further modelling was done where the fuels were modelled in equilibrium with the OC at 800 °C -the approximate operating temperature of the FR. Since the amount of OC that actually reaches equilibrium with the fuel in the actual CLC system is not possible to determine, the amount of OC was left as the independent free variable in the FactSage simulation. The simulation was then run for various values of  $R_{OC/F}$  - the mass ratio of the OC that is in equilibrium with the fuel. Since in CLC, the OC is responsible for providing the oxygen for fuel conversion, increasing the  $R_{OC/F}$  parameter increases the overall gas conversion,  $\eta_{g.c.}$ . The model was run up to the point where  $\eta_{g.c.}$  reached 90%. This represents the upper limit of the gas conversion that has been reported for CLC operation with various biomass fuels [14,21,59–61]. The equilibrium distribution of K-containing species is shown in Figs. 9 and 10 for WP and WC fuels in equilibrium with ilmenite. In these figures, K-species are plotted against the  $R_{OC/F}$  parameter. The values of gas conversion,  $\eta_{g.c.}$ , calculated from the equilibrium concentrations of CO,  $CO_2$ ,  $CH_4$  and  $H_2$  as per Eq. 2, are also shown in the figure. It should be noted that for  $R_{OC/F} = 0$ ,  $\eta_{g.c.}$  is above 20% due to equilibrium between the fuel's own oxygen content with the rest of the fuel constituents. For clarity, the condensed and gaseous species in Figs. 9 and 10 are shown on different sub-plots. Also, the figures are truncated, showing data up to the point where K speciation no longer changes with increasing  $R_{OC/F}$ . Beyond this point, the K speciation remains unchanged right up to the practical operating limit of  $\eta_{g.c.}$  of 90%.

Figs. 9 and 10 show that the gaseous K-species present in equilibrium of fuel with ilmenite are  $KOH(g)$  and  $KCl(g)$ . A minor amount of  $K(g)$  is also predicted to be stable at low  $R_{OC/F}$  values for WP fuel. As the  $R_{OC/F}$  value increases, the stability of the gaseous K species is affected. For WP fuel,  $KOH(g)$  and  $K(g)$  stability decreases rapidly at higher  $R_{OC/F}$  values.  $KCl(g)$  stability also decreases, but at a much lower rate. The decrease in gaseous alkali stability is accompanied with formation of condensed-phase K species, such as a slag phases, K-silicates, and K-Al-silicates. Figs. 9 and 10 include the values of gas conversion efficiency,  $\eta_{g.c.}$ , that would result from full equilibrium for the fuel and OC. The value of  $\eta_{g.c.}$

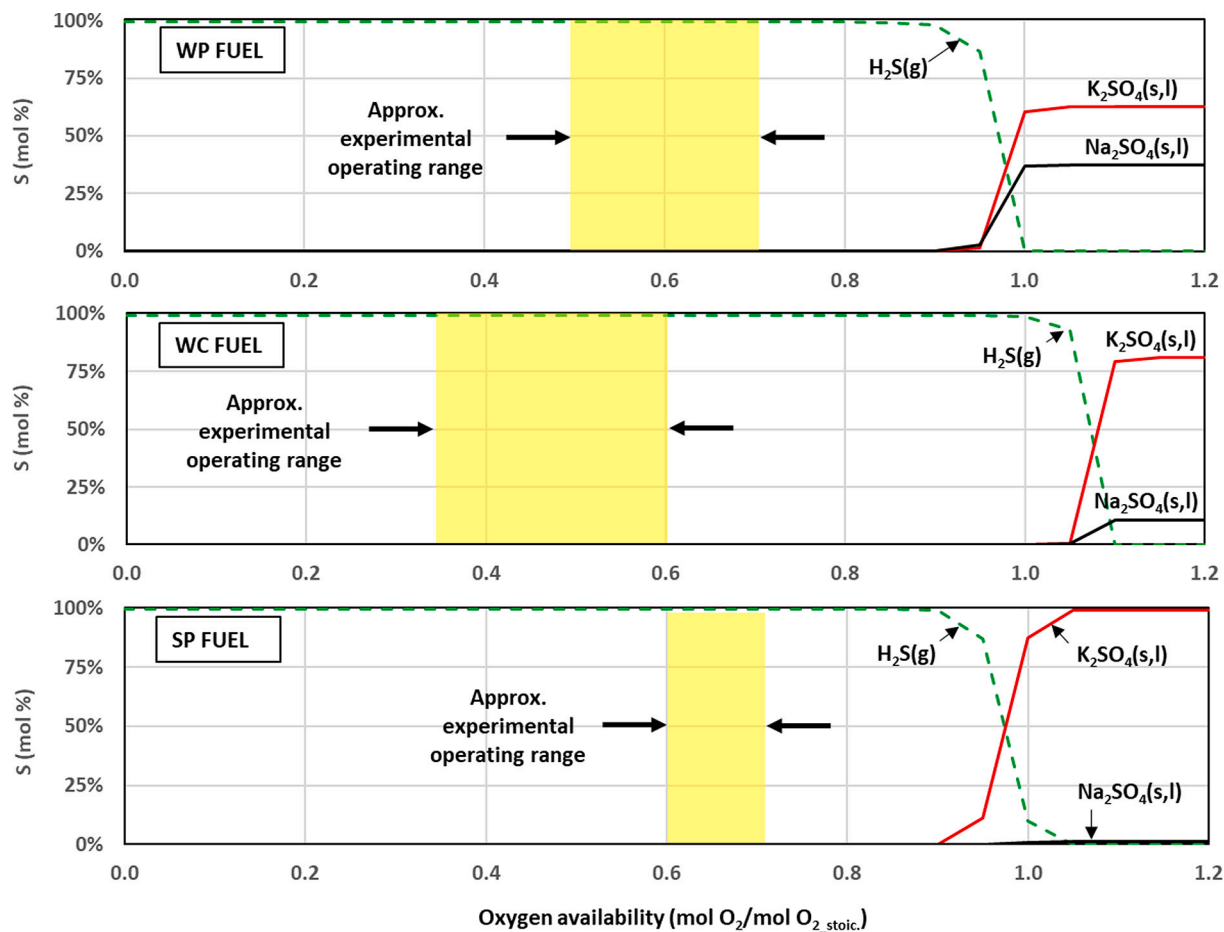


Fig. 8. Sulfur species stability vs. oxygen availability.

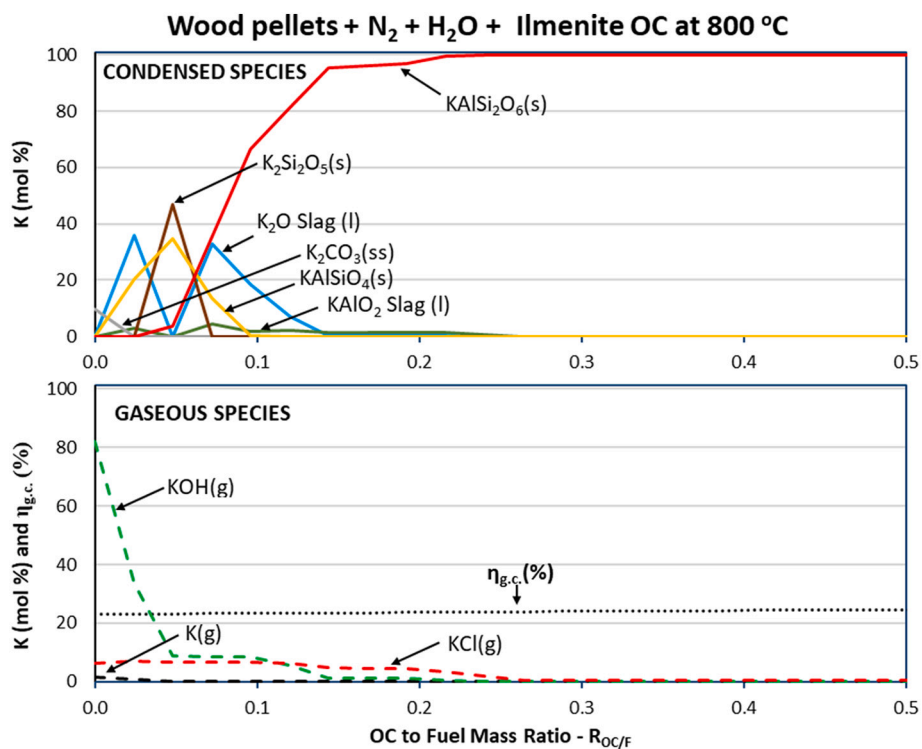


Fig. 9. Equilibrium K-species for wood pellets fuel reaction with ilmenite OC.

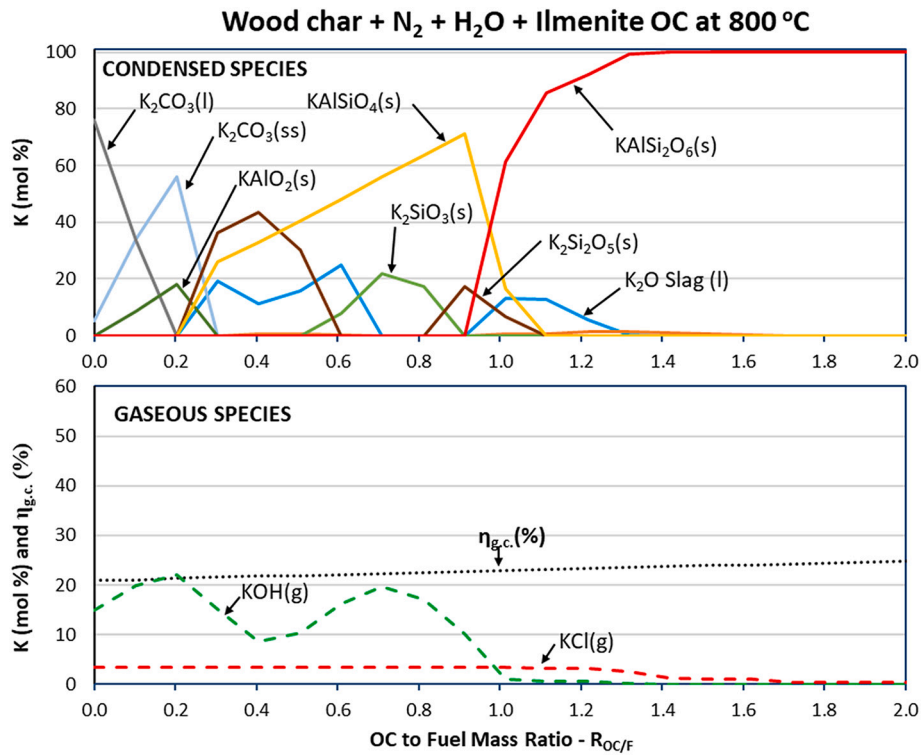


Fig. 10. Equilibrium K-species for wood char fuel reaction with ilmenite OC.

increases with higher  $R_{OC/F}$ , as more oxygen-carrying ilmenite is available for reaction. At  $R_{OC/F} > 0.25$ , which corresponds to  $\eta_{g.c.} > 24\%$ ,  $KOH(g)$  and  $KCl(s)$  levels decay to trace amounts, and the majority of K is predicted to be incorporated as  $KAlSi_2O_6(s)$ . Thus, at the  $\eta_{g.c.}$  levels experienced in the conducted CLC experiments (see Table 5), only trace amounts of  $KOH(g)$  and  $KCl(g)$  are predicted to be in the gas phase. The case for WC fuel is similar, even though the decay of  $KOH(g)$  stability is less drastic and is predicted to vary for  $R_{OC/F} < 1$ . For WC fuel, for  $R_{OC/F}$

$> 1.4$ , which corresponds to  $\eta_{g.c.} > 24\%$ , nearly all K is predicted to be held as  $KAlSi_2O_6(s)$ , with minor amount of  $KOH(g)$  and  $KCl(g)$  in the gas phase. Unfortunately, the condensed phases predicted by the model cannot be verified as there is no comparative data on what alkali species formed in CLC operation. However, the general trend presented by the model makes sense. Since ilmenite contains Si and Al, higher ratio of ilmenite in equilibrium with the fuels means more availability of Si and Al to form  $KAlSi_2O_6(s)$ . The large proportion of K that is predicted to

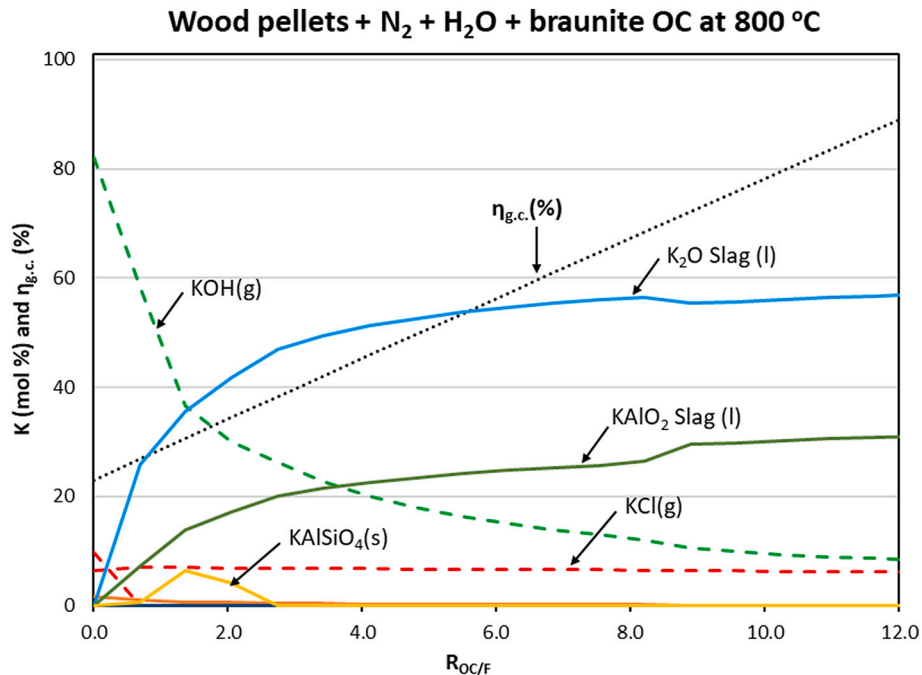


Fig. 11. Equilibrium K-species for wood pellets fuel reaction with braunite OC.



form silicates is consistent with the significant absorption of alkalis confirmed from a SID-based mass balances performed during this campaign [22], and previous CLC campaigns with ilmenite OC [21,22,59].

The equilibrium distribution of K-containing species is shown for WP, WC, and SP fuels in equilibrium with braunite OC in Figs. 11 through 13.

Figs. 11 through 13 show that FactSage modelling predicts that braunite has a different effect than ilmenite on gaseous alkali species. Unlike for ilmenite, increasing the amount of braunite in equilibrium for each of the three biomass fuels does not seem to significantly affect the stability of  $\text{KCl(g)}$  and  $\text{(KCl)}_2\text{(g)}$ . Thus, the model indicates that braunite is not likely to affect KCl release to the gas-phase. For  $\text{KOH(g)}$  the case is different. Increasing the amount of braunite in equilibrium with the fuel reduces  $\text{KOH(g)}$  stability. This effect is quite significant for the WP fuel, but mild for the WC and SP fuels. As in the ilmenite case, decrease in  $\text{KOH(g)}$  stability is mirrored by the growth in stability of condensed-phase K species. FactSage predicts  $\text{K}_2\text{O}$  and  $\text{KAlO}_2$  slag phases to incorporate more K with increasing  $R_{\text{OC/F}}$  for WP and WC fuels. For the SP fuel, incorporation of K into a condensed phase is predicted to be dominated by formation of  $\text{KAlSiO}_4$ , followed by  $\text{K}_2\text{O}$  and  $\text{KAlO}_2$  slag phases. As in the ilmenite case, due to lack of reference data on interaction of K with braunite OC at CLC conditions, the predicted phases cannot be verified. For the  $\eta_{\text{g.c.}}$  values achieved in the CLC pilot experiments, the model predicts that  $\text{KOH(g)}$  should be the dominant gaseous K specie for WP and WC fuel tests, and  $\text{KCl(g)}$  should be dominant in the SP fuel tests. It should be noted that in comparison to ilmenite, braunite is predicted to exhibit lower capture of K, and thus should lead to an overall higher release of gaseous K species. This is consistent with the SID-based and impactor based measurements reported in Sections 4.3 and 4.4.

In summary, thermodynamic modelling shows that fuel conversion with ilmenite should result in capture of most of the fuel K as K-silicates, preventing significant release of  $\text{KCl(g)}$  and  $\text{KOH(g)}$  gas species. Fuel conversion with braunite should result in capture of significant proportion of the fuel K as K-silicates or in slag phases, but should not significantly limit the gas-phase release of K as  $\text{KCl(g)}$  or  $\text{(KCl)}_2\text{(g)}$ .

#### 4.2.3. Alkali distribution prediction for impactor sampling periods

Prediction of the alkali species distribution was performed in FactSage for impactor sampling periods DLPI 1 to DLPI 5. The operating conditions during the impactor sampling periods are summarized in Table 5. These parameters were used as input to the FactSage model for each of the sampling cases. The prediction results are presented in Figs. 14 and 15, for K and Na, respectively. A data table summarizing the predicted amount of each K/Na species, expressed in mol K/Na per kg of fuel, is included for each of the figures.

The model results in Fig. 14 show that for WP and WC fuel tests with ilmenite OC, >99% of the fuel K is predicted to be retained in condensed phases. Very little gaseous release is expected, with most of the gaseous release occurring as  $\text{KCl(s)}$ . The high retention percentage predicted by the model is in reasonable agreement with >96% alkali retention calculated from SID alkali measurements during the same experimental campaign [22], and retention figures of >90% [21] and > 92% [62] reported in previous CLC experiments with ilmenite OC. For operation with braunite, retention of K in condensed phases is predicted to be >80%, which is lower than the ilmenite case. Braunite's lower alkali capture ability was also confirmed from estimates on alkali retention calculated from SID alkali measurements, as well as solids sample analyses performed in the same experimental campaign [22]. With lower capture of alkalis in condensed phases, gaseous K release is predicted to be higher. Most gaseous K is predicted to be released as  $\text{KOH(g)}$ , followed by a lower share of  $\text{KCl(g)}$ . For the SP fuel, gaseous release is predicted to be approximately 27% of the fuel K, with retention of K in condensed phases of >70%. Gaseous release for SP fuel is predicted to be dominated by  $\text{KCl(g)}$ , followed by  $\text{(KCl)}_2\text{(g)}$ , and trace amounts of  $\text{KOH(g)}$  and  $\text{K(g)}$ . The condensed species that capture K are predicted to be different for ilmenite and braunite. For ilmenite,  $\text{KAlSi}_2\text{O}_6$  is predicted to account for almost all of the retention. For braunite, K is predicted to be retained in a slag phase for WP and WC fuels, and as  $\text{KAlSiO}_4$  and a slag phase for the SP fuel.

For Na, Fig. 15 shows a similar trend as for K, but for WP and WC fuels the retention of Na by braunite is predicted to be significantly higher than braunite's retention of K. The SP fuel case also seems different, with gaseous release of Na predicted to be >80% of the fuel's Na content. As for the case for K retention, ilmenite and braunite are predicted to capture Na in different condensed-phase species. For

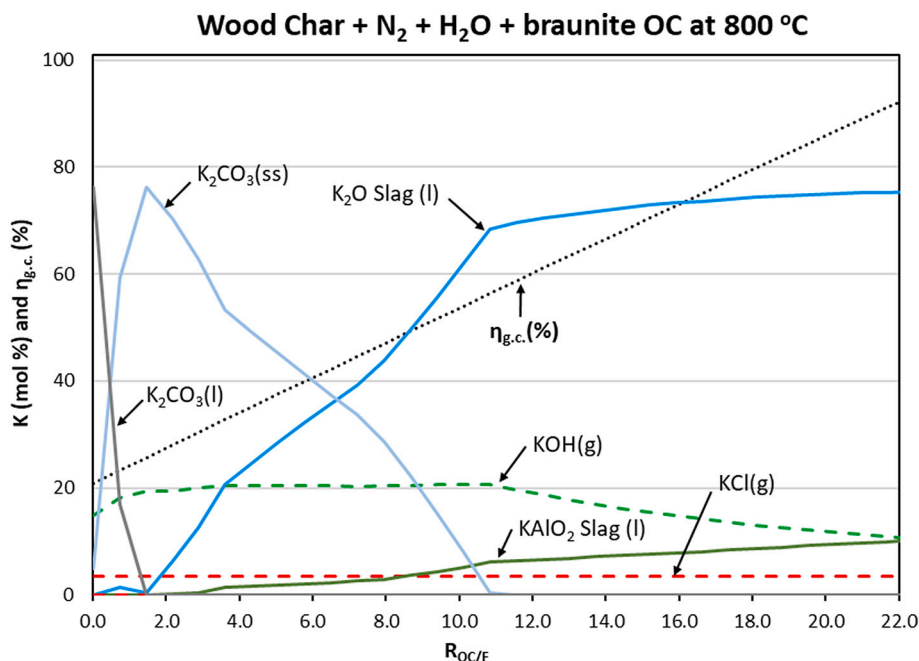


Fig. 12. Equilibrium K-species for wood char fuel reaction with braunite OC.

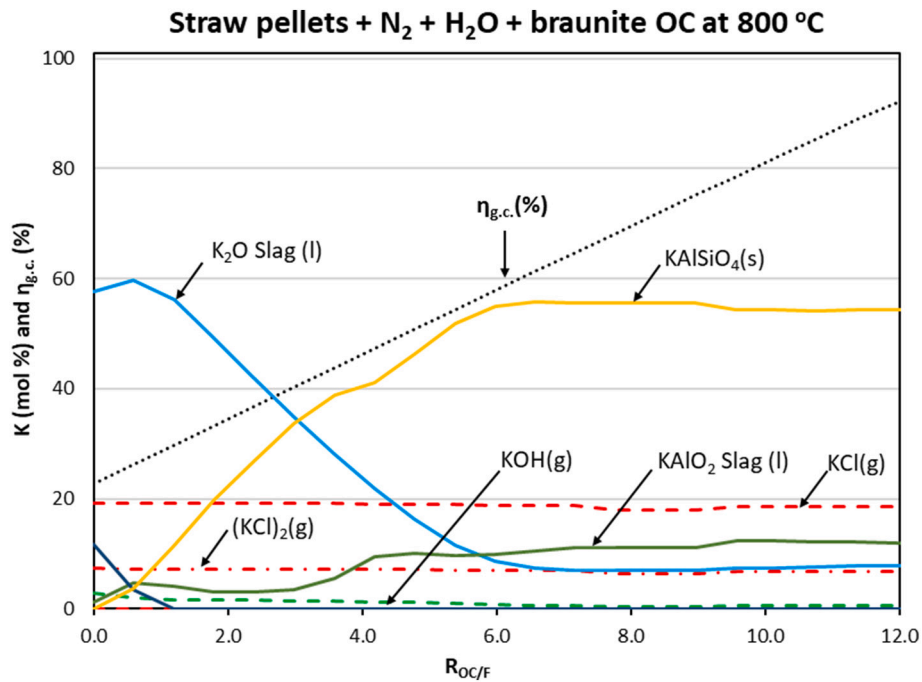


Fig. 13. Equilibrium K-species for straw pellets fuel reaction with braunite OC.

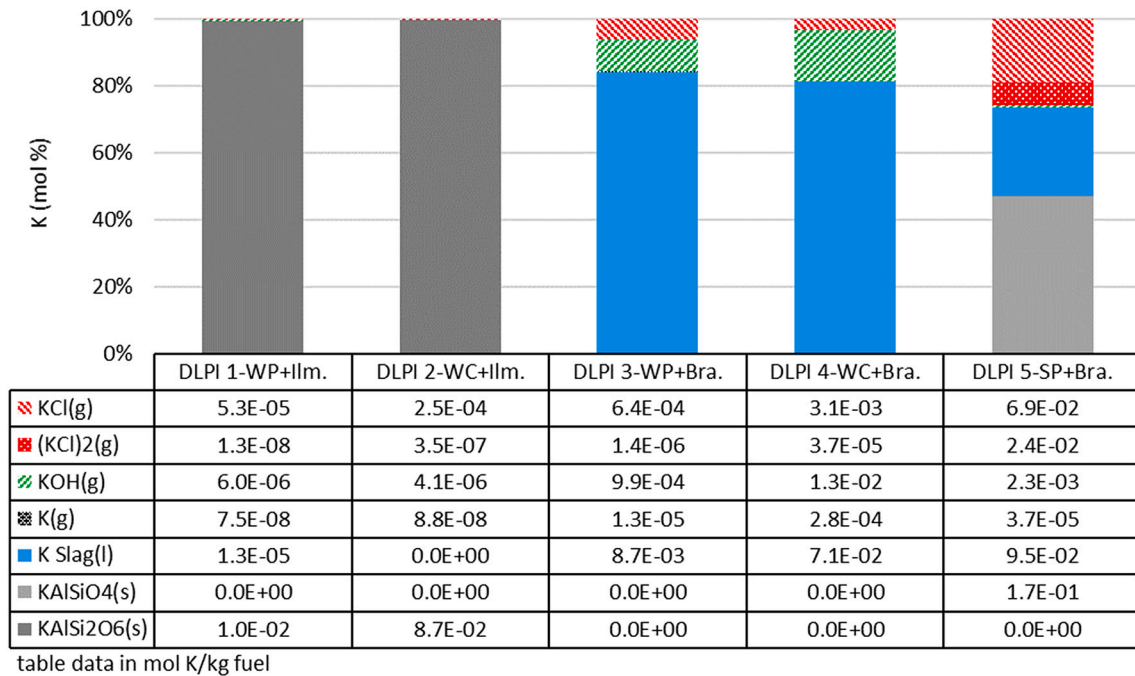


Fig. 14. Predicted equilibrium K distribution for impactor test periods DLPI 1 - DLPI 5.

ilmenite, NaAlSiO<sub>4</sub> is a dominant specie. For braunite, Na is predicted to be captured entirely in a Na slag phase. This indicates that Na has a lower affinity for silicate formation, when compared to K.

#### 4.3. DLPI sample Leachate analysis

The alkali content of the collected ash samples was investigated by leaching the DLPI samples in water and analyzing the leachate for cations with ICP-MS and for anions with IC. ICP-MS analysis included detection of K, Na, Ca, Mg, Ti, Al, Si, Fe, Mn, and Zn. IC analysis included detection of Cl and SO<sub>4</sub>. Fig. 16 presents the concentrations of K, Na, and

Zn cations, and Cl and SO<sub>4</sub> anions for all of the DLPI samples. Zn is included since ZnCl<sub>2</sub> is common volatile ash specie that takes up the Cl anion, which is otherwise mostly associated with K and Na. Mg, Mn, Ti, Al, Si, and Fe cations were excluded since thermodynamic modelling showed that these cations do not form substantial amounts of alkali species, or form alkali species which are not soluble in water. Interpretation of the leachate composition results relied on assumptions of element association that were established in thermodynamic modelling. These assumptions were:

- If Cl is available, K and Na prefer association as KCl and NaCl

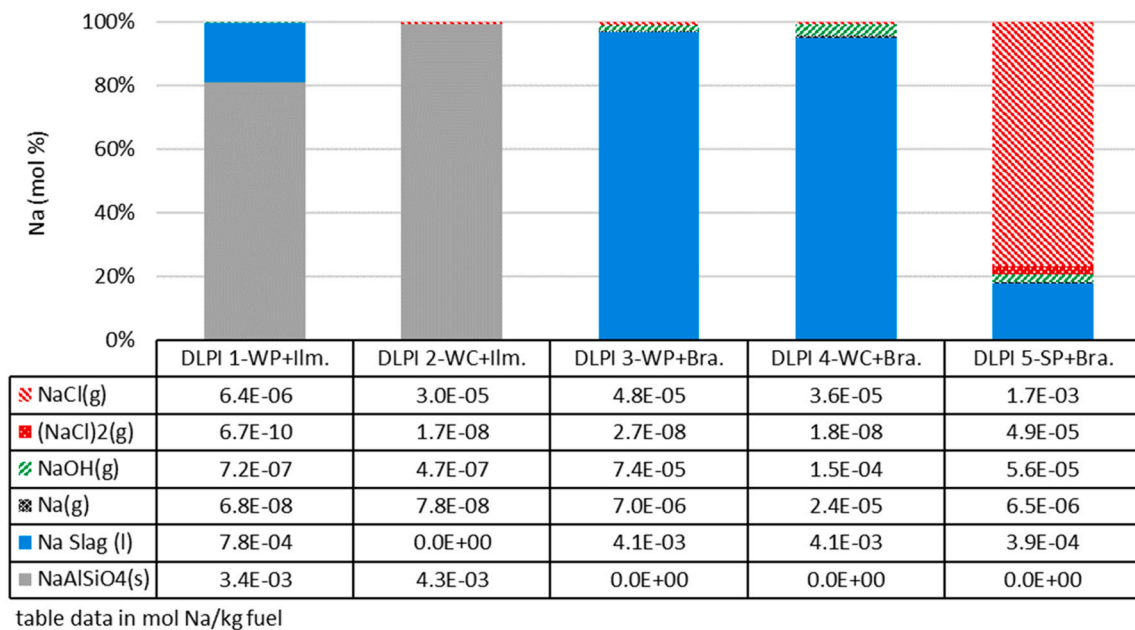


Fig. 15. Predicted equilibrium Na distribution for impactor test periods DLPI 1 - DLPI 5.

- K and Na present in excess of Cl are associated as KOH and NaOH
- K and Na association with the  $\text{SO}_4$  anion is unlikely

The last assumption is based on the fact that thermodynamic modelling presented in Section 4.2.1 showed that K and Na-sulphates are not stable due to the highly reducing conditions experienced in the CLC experiments (see discussion around Fig. 8).

Fig. 16a shows that no alkali species are detected for CLC of WP fuel with ilmenite oxygen carrier. This is consistent with the modelling results in Fig. 14, where most of the alkalis are predicted to be retained as alkali silicates. Minor amounts of Zn are detected in both fine and coarse particles. In the coarse mode, Zn is found along with Cl, indicating  $\text{ZnCl}_2$  presence in the fly ash. For WP fuel operation with braunite OC, Fig. 16c shows that K is detected along with Cl in approximately equimolar amounts in the smallest particle size fraction ( $<0.03 \mu\text{m}$ ), suggesting KCl presence. K and Na are detected along with Cl and  $\text{SO}_4$  in the  $0.6\text{--}2.4 \mu\text{m}$  fraction. As mentioned prior, association of K and Na with  $\text{SO}_4$  is deemed to be unlikely on the basis of thermodynamic modelling results. Thus, alkalis from the leaching tests are likely present as KCl and NaCl, as well as KOH and NaOH for K and Na that is in stoichiometric excess to Cl.

For WC fuel, Fig. 16b and d show that K is found in the coarse fraction in association with Cl for ilmenite and braunite cases. In both cases, K is present in concentrations several times higher than Cl, suggesting that higher proportion of K associated as KOH, than KCl. For WC fuel with braunite OC, this qualitatively matches the model prediction for the DLPI 4 case in Fig. 14. For WC fuel with ilmenite OC, modelling results predict KCl dominance of KOH, while the opposite is suggested in Fig. 16b. In comparing Fig. 16b and d, it should be noted that K concentration in the flue gas is over 5 times higher in operation with braunite, when compared to ilmenite. This large difference is consistent with the large difference in gas-phase alkali release predicted by the model results in Fig. 14. This difference in gas-phase release in operation with different oxygen carriers further confirms that ilmenite is capturing K that is released to the gas phase during WC fuel conversion.

For operation of SP fuel with braunite OC, Fig. 16e and f show significant levels of K and minor levels of Na in association with Cl. The molar amounts of K and Na correspond to the measured molar amounts of the Cl anion, suggesting that the majority of alkalis collected in the impactor are KCl and NaCl. This is consistent with the modelling results for the DLPI 5 case in Figs. 14 and 15, where most gas-phase alkalis are

predicted to be dominated by KCl and NaCl. Unlike for WP and WC fuels, for the SP fuel, K, Na, and Cl are almost fully present in the fine particle mode. A surprising observation is that high alkali levels are present in both the FR (Fig. 16e) and AR (Fig. 16f) samples. This, however, can be explained by the relatively poor carbon capture performance of the CLC reactor system. Typically, CLC pilots of a similar size to the one used in the current study achieve carbon capture efficiencies of  $>97\%$  [20,21]. For the D-FBC pilot used in this study, carbon capture efficiency was approximately 80% for operation with SP fuel and braunite OC. This means that approximately 20% of the fuel's total carbon was carried over from the FR to the AR. Since biomass undergoes devolatilization in the FR, carbon carryover from the AR to the FR almost certainly occurs as char carryover. Given the SP fuel's total and fixed carbon content (43.2 wt% total carbon, 17.1 wt% fixed carbon), 20% carryover of the fuel's total carbon content corresponds to a carryover of approximately half of the fuel char from the FR to the AR. As mentioned in Section 2.2, char that forms from fuel devolatilization can contain  $>90\%$  of the fuel's alkali content. As such, the high AR alkali emissions shown in Fig. 16f can be explained by the high levels of char slip that occurred during operation.

Impactor analysis results presented in Fig. 16 were recalculated to alkali specie mass concentrations. The relative distributions of the detected alkali species are summarized in Fig. 17. Fig. 17 data table shows the alkali species mass concentrations as well as the weight fraction of the total DLPI particle sample that the detected alkali species constitute. In Fig. 17, the DLPI 1 case is now shown, as no alkalis were detected in that sample.

Fig. 17 shows that for WP and WC fuel operation, alkali compounds occur mostly in the coarse fraction. The alkalis also make up a very small portion of the total particle sample mass, meaning that the vast majority of the particles captured in the impactor consist of non-volatile ash species. Both of these observations suggests that the alkali species undergo heterogeneous nucleation, condensing on existing seed particles, rather than forming particles through homogeneous nucleation. This observation is in line with the findings of Jensen et al. [63]. In their study, Jensen et al. showed that at high rates of seed particles, homogeneous nucleation of alkali particles is suppressed, resulting in primarily a monomodal particle size distribution. This indeed is the case in the WP and WC tests where high concentrations of particles with low proportion of alkali content results in the monomodal distributions seen in Figs. 4b,

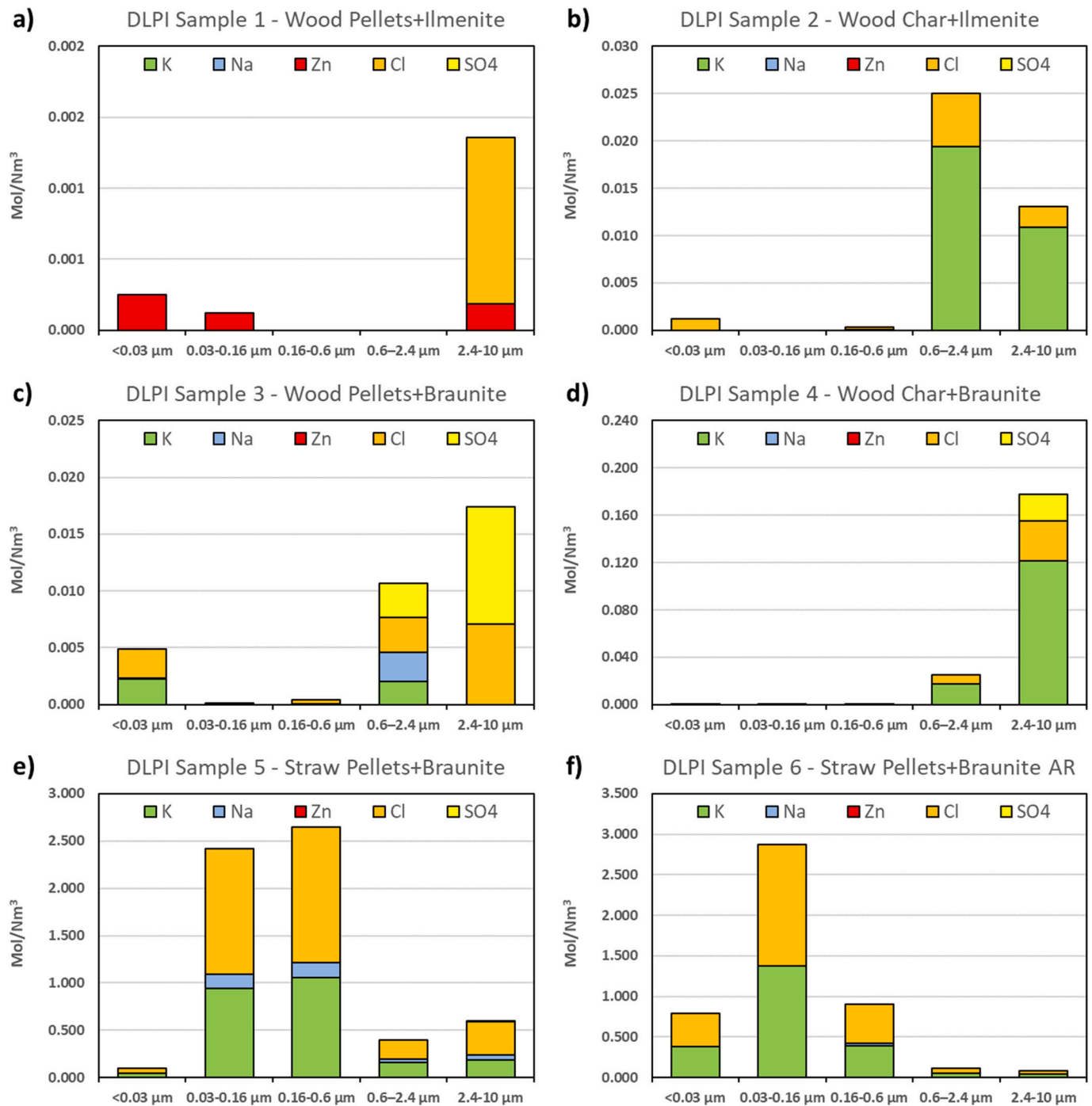


**Fig. 16.** Water leachate composition for a) wood pellets and ilmenite CLC – FR fly ash, b) wood char and ilmenite CLC – FR fly ash, c) wood pellets and braunite CLC – FR fly ash, d) wood char and braunite CLC – FR fly ash, e) straw pellets and braunite CLC – FR fly ash, f) straw pellets and braunite CLC – AR fly ash.

c, and d. Formation of alkali particles through homogeneous nucleation is much more likely in the SP fuel case. In DLPI 5 and DLPI 6 cases, KCl is the dominant alkali species and occurs in the fine particle mode. KCl also makes up most of the sample weight in the fine particle mode. This indicates that the fine particles are mostly formed by homogeneous nucleation of KCl. These fine KCl particles result in the fine particle mode, whereas non-alkali ash species form the coarse particle mode of the bimodal distributions seen in Fig. 4e and f.

#### 4.4. Comparison of modelling and sampling results

In addition to determining the mass concentration and speciation of

alkali species, the secondary aim of this work was to compare two methodologies for measurement and evaluation of gas-phase alkali emissions in CLC. As mentioned prior, surface ionization detector (SID) measurements were also collected during the impactor sampling periods. A comparison of FactSage modelling predictions, the SID-based alkali measurements, and the impactor-based alkali measurements are presented in Fig. 18.

Fig. 18 shows that for operation with ilmenite, FactSage modelling predictions lie between impactor and SID results. For operation with braunite, model results are much higher than SID and impactor results. Since solid fuel conversion is a complex process, the model's departure from SID and impactor measurements is most likely a result of the



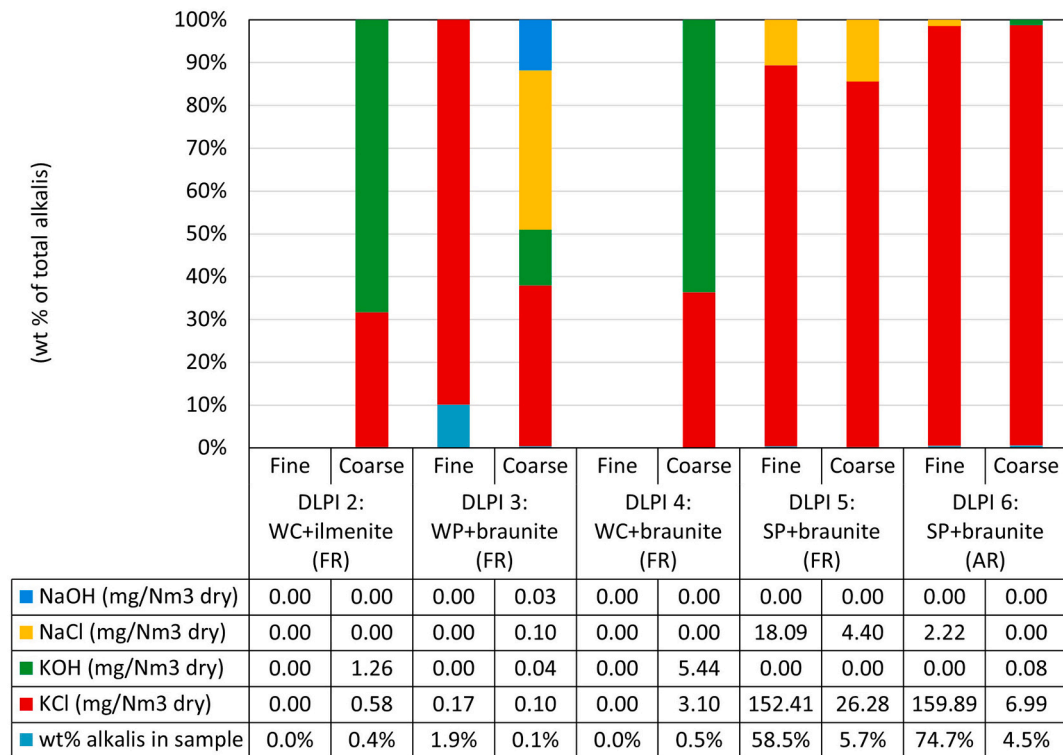


Fig. 17. Impactor sample alkali speciation.

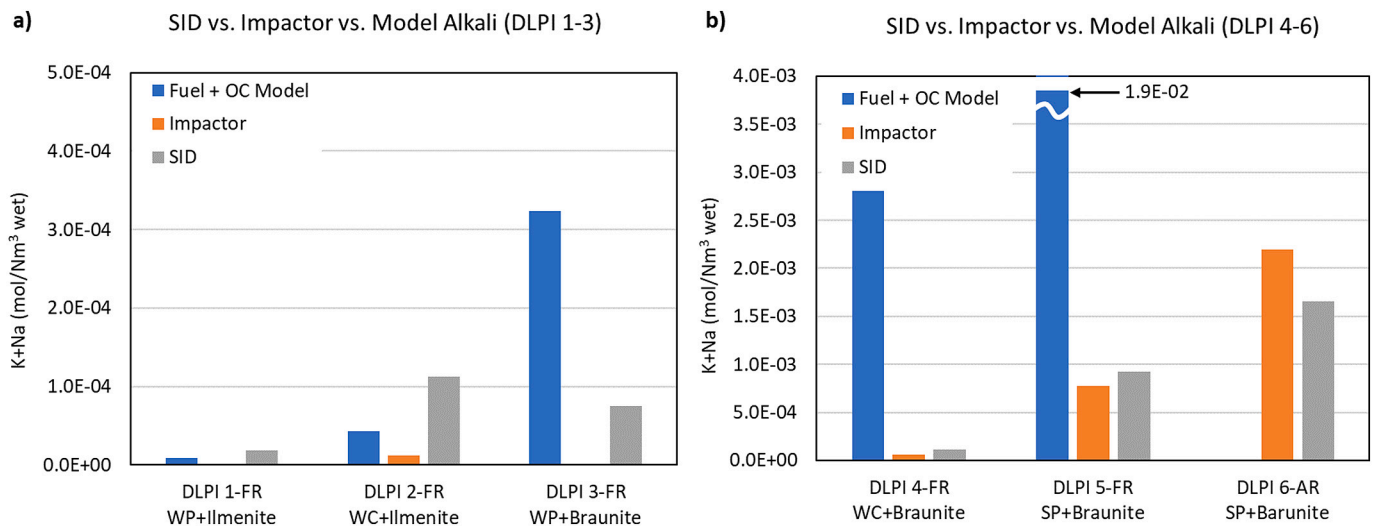


Fig. 18. Comparison of model prediction vs. SID and impactor gas-phase alkali measurements for a) sampling periods DLPI 1 – DLPI 3 b) sampling periods DLPI 4 – DLPI 6.

oversimplifying assumptions of perfect mixing and no kinetic limitations that are implicit in FactSage modelling. Modelling results, however, agree with the qualitative trends of higher emissions for higher alkali content fuels, and higher emissions with braunite vs. ilmenite for WP and WC operation.

In comparing SID and impactor results, Fig. 18a shows that for samples DLPI 1 through DLPI 3, the SID reports a much higher level of alkalis than the impactor measurements. The likely explanation for low impactor concentrations is that the sampling times used in the experiments were not long enough for the impactor to collect a sufficient sample mass. Selection of short sampling times is a well-known issue for impactor measurement of dilute streams, such as in sample periods DLPI

1 through DLPI 3. Unfortunately, selection of appropriate impactor sampling times is extremely difficult, as it is done prior to knowing the flue gas conditions. Unlike the impactor system, the SID instrument has been demonstrated to have very high sensitivity to alkalis in a wide range of flue gas conditions [64–67]. As such, SID results for samples DLPI 1 through DLPI 3 are likely more representative of the actual flue gas alkali levels. The SID results show that emissions for WC fuel are several times higher than for WP fuel. This is consistent with the fact that WC fuel's alkali content is several times higher than that of WP fuel. This is also consistent with the relative difference in the alkali levels predicted by the FactSage model. SID emissions for WP operation with ilmenite are lower than for WP fuel operation with braunite OC. This is

consistent with results discussed in Section 4.2.2 that show that FactSage modelling predicts that ilmenite has a stronger effect on limiting gas-phase alkali emissions through forming stable condensed-phase alkali compounds.

Fig. 18b shows results for samples DLPI 4 through DLPI 6. In these samples the flue gas alkali concentrations are higher, especially in operation with SP fuel in samples DLPI 5 and DLPI 6. With higher alkali concentrations, the impactor results become more accurate and are in reasonable agreement with SID measurement results. The SID and impactor results, as well as the modelling predictions, clearly indicate a significant rise in alkali emission between WC operation in sample DLPI 4 and SP operation in sample DLPI 5. Surprisingly, the highest emissions levels are reported for sample DLPI 6, where the AR flue gas is measured for alkali content during FR operation with SP fuel. As discussed in Section 4.3, the AR emissions are a result of significant carryover of char from the FR to the AR.

In conclusion, in comparing SID and impactor alkali emissions measurement methodologies, it is clear that neither method on its own is sufficient for establishing a clear picture of alkali behavior in CLC. Each methodology has its strengths and weaknesses. Impactor measurements have the advantage of being able to quantify and identify alkali species. However, impactor sampling was shown to be ineffective for collecting alkali particles from flue gases of dilute alkali concentrations. Furthermore, interpretation of impactor sample leaching results relies on thermodynamic modelling predictions for identifying what species K and Na form with other elements found in the flue gas. Finally, impactor sampling provides only average emissions figures and is not well suited for reflecting alkali emissions changes that result from transient events. The SID technique, on the other hand, is an online alkali emissions measurement methodology. It has the advantage of being able to show how changes in operating parameters affect alkali emissions. This capability was demonstrated in earlier studies [21,22,62,68]. Another advantage of the SID technique is that it has a high sensitivity towards alkalis [64,65,69]. The disadvantage of the SID technique is that the SID cannot differentiate between different alkali species, and thus cannot be used for speciation of alkali emissions. Lastly, it should be noted that the FactSage thermodynamic model provides inadequate quantitative predictions, but provides valuable qualitative information on gaseous alkali speciation and the potential effects of the oxygen carriers on alkali release. Thus, FactSage modelling is a useful complementary methodology for SID and impactor alkali measurement techniques.

## 5. Conclusions

Chemical looping combustion of biomass fuels was carried out in a 60 kW dual circulating fluidized bed CLC pilot. Three biomass fuels (WP-wood pellets, WC-wood char, SP-straw pellets) were tested with two different oxygen carriers (ilmenite, braunite). An impactor-based measurement system was used to sample the flue gas streams from the FR (for all tests) and the AR (for the SP-braunite test). The impactor measurements were used for determination of particle mass size distributions. The particles collected in the impactor system were leached in water, and the leachate was analyzed to identify the alkali species present in the sample. To aid in interpreting impactor results, FactSage 7.2 thermodynamic modelling software was used to predict stable alkali species that occur in conversion of the biomass fuels at CLC process conditions. Concurrently with the impactor measurements, alkali emissions were also measured with a surface ionization detector (SID).

Thermodynamic modelling for fuel conversion with oxygen and steam at 800 °C showed that for WP and WC fuels, equilibrium K species are dominated by KOH(g), followed by lower concentrations of KCl(g). For the SP fuel, which contains higher amounts of K, Cl, but also Si, equilibrium K species are dominated by condensed-phase K species, followed by gas-phase KCl(g), (KCl)<sub>2</sub>(g), and KOH(g), in order of decreasing dominance. Modelling of the effect of the oxygen carriers showed that concentrations of KOH(g) and KCl(g) fall, while

concentrations of condensed-phase K species rise with increased proportion of ilmenite in equilibrium with the fuels. For braunite, this effect was milder, and increased condensed-phase K stability was accompanied with a decrease of KOH(g) only. Equilibrium KCl(g) concentrations were unaffected by fuel equilibrium with the braunite OC.

Impactor measurements showed that particle mass concentration correlated with the fuel's total ash content. The highest particle mass concentration occurred in operation with WC fuel, followed by SP fuel, and WP fuel, respectively. Particle size distribution analysis showed that operation with WP and WC fuels were dominated by coarse particles (>1 µm) that are known to be formed by refractory ash species, rather than alkali species. The particle size distribution for operation with straw was bimodal, with the distinct fine particle mode (<1 µm) formed from nucleation of volatile ash species, such as alkalis.

Impactor sample leachate analysis showed that for operation with ilmenite and WP fuel, no alkalis were detected. For WP operation with braunite, the sample contained KCl, NaCl, KOH, and NaOH, in order of decreasing concentration. For WC operation with ilmenite, the samples contained KOH and KCl, in order of decreasing concentration. For SP fuel operation, leachate analysis showed that almost all of the alkalis detected occur as KCl. Analysis of the sample weight contribution and the size fractions where most alkali species were found, concluded that alkali species undergo heterogeneous nucleation in WP and WC fuel operation, whereby gaseous alkali species condense onto existing refractory fly ash particles. For SP fuel operation, alkali condensation was determined to occur via homogeneous nucleation, forming submicron alkali fly ash particles. In terms of gaseous alkali release quantity, the impactor measurements and modelling predictions showed that higher gaseous release occurs for SP, WC, and WP fuels, respectively. Impactor measurements and modelling results also showed that a larger share of the fuels' alkali content is released with braunite vs. ilmenite OC.

Flue gas alkali concentrations determined from the impactor samples were compared to alkali concentrations measured by the SID-based alkali measurement system. For operation of WP and WC fuels with ilmenite, and operation of WP fuel with braunite, the SID and impactor results were vastly different. Of the two methods, the impactor results were determined to be less quantitatively reliable due to insufficient sampling durations at the low flue gas alkali concentrations. For operation of WC and SP fuel with braunite, where flue gas alkali concentrations are higher, the impactor measurements were in reasonable agreement with the SID results. In comparison of the two alkali measurement techniques, key advantages of each method were identified. The SID is more sensitive than the impactor technique and can be used for online alkali detection. The impactor method, on the other hand, can be used to determine alkali speciation. The use of both techniques can benefit from support provided by thermodynamic modelling.

## CRedit authorship contribution statement

**Ivan Gogolev:** Conceptualization, Methodology, Software, Validation, Formal analysis, Investigation, Resources, Data curation, Writing – original draft, Writing – review & editing, Visualization. **Toni Pikkarainen:** Conceptualization, Methodology, Investigation, Resources, Writing – review & editing, Supervision, Project administration, Funding acquisition. **Juho Kauppinen:** Methodology, Formal analysis, Investigation, Writing – review & editing. **Markus Hurskainen:** Methodology, Formal analysis, Investigation. **Anders Lyngfelt:** Writing – review & editing, Supervision, Project administration, Funding acquisition.

## Declaration of Competing Interest

The authors declare that they have no known competing financial interests or personal relationships that could have appeared to influence the work reported in this paper.

## Data availability

Data will be made available on request.

## Acknowledgements

This work was carried out with funding from Swedish Research Council, project “Biomass combustion chemistry with oxygen carriers” (contract 2016-06023), and funding from Nordic Energy Research, flagship project “Negative CO<sub>2</sub> emissions in the Nordic system” (project No. 77.732).

## References

- [1] X. Zhao, H. Zhou, V.S. Sikarwar, M. Zhao, A.-H.A. Park, P.S. Fennell, et al., Biomass-based chemical looping technologies: the good, the bad and the future. *Energy, Environ. Sci.* 10 (2017) 1885–1910, <https://doi.org/10.1039/C6EE03718F>.
- [2] M.M. Hossain, H.I. de Lasa, Chemical-looping combustion (CLC) for inherent CO<sub>2</sub> separations—a review, *Chem. Eng. Sci.* 63 (2008) 4433–4451, <https://doi.org/10.1016/j.ces.2008.05.028>.
- [3] S. Abuelgasim, W. Wang, A. Abdalazeez, A brief review for chemical looping combustion as a promising CO<sub>2</sub> capture technology: Fundamentals and progress, *Sci. Total Environ.* 764 (2021), 142892, <https://doi.org/10.1016/j.scitotenv.2020.142892>.
- [4] T. Song, L. Shen, Review of reactor for chemical looping combustion of solid fuels, *Int J Greenh Gas Control* 76 (2018) 92–110, <https://doi.org/10.1016/j.ijggc.2018.06.004>.
- [5] A. Lyngfelt, Chemical looping combustion: status and development challenges, *Energy Fuel* 34 (2020) 9077–9093, <https://doi.org/10.1021/acs.energyfuels.0c01454>.
- [6] A. Coppola, F. Scala, Chemical looping for combustion of solid biomass: a review, *Energy Fuel* 35 (2021) 19248–19265, <https://doi.org/10.1021/ACS.ENERGYFUELS.1C02600/ASSET/IMAGES/MEDIUM/EF1C02600.0010.GIF>.
- [7] A. Lyngfelt, C. Linderholm, Chemical-looping combustion of solid fuels - status and recent progress, *Energy Procedia* 114 (2017) 371–386, <https://doi.org/10.1016/j.egypro.2017.03.1179>.
- [8] H. Gu, L. Shen, J. Xiao, S. Zhang, T. Song, Chemical looping combustion of biomass/coal with natural iron ore as oxygen carrier in a continuous reactor, *Energy Fuel* 25 (2011) 446–455, <https://doi.org/10.1021/ef101318b>.
- [9] H. Gu, L. Shen, Z. Zhong, Y. Zhou, W. Liu, X. Niu, et al., Interaction between biomass ash and iron ore oxygen carrier during chemical looping combustion, *Chem. Eng. J.* 277 (2015) 70–78, <https://doi.org/10.1016/j.cej.2015.04.105>.
- [10] I. Adánez-Rubio, A. Abad, P. Gayán, L.F. De Diego, F. García-Labiano, J. Adánez, Biomass combustion with CO<sub>2</sub> capture by chemical looping with oxygen uncoupling (CLOU), *Fuel Process. Technol.* 124 (2014) 104–114, <https://doi.org/10.1016/j.fuproc.2014.02.019>.
- [11] T. Mendiara, A. Abad, L.F. de Diego, F. García-Labiano, P. Gayán, J. Adánez, Biomass combustion in a CLC system using an iron ore as an oxygen carrier, *Int J Greenh Gas Control* 19 (2013) 322–330, <https://doi.org/10.1016/j.ijggc.2013.09.012>.
- [12] T. Pikkariainen, I. Hiltunen, Chemical Looping Combustion of Solid Biomass—Performance of Ilmenite and Braunitz as Oxygen Carrier Materials, 2017.
- [13] Ø. Langengen, I. Saanum, Chemical Looping Combustion of wood pellets in a 150 kW th CLC reactor, *Proc. Int. Conf. Negat. CO<sub>2</sub> Emiss.* (2018) 1–10.
- [14] M. Schmitz, C. Linderholm, Chemical looping combustion of biomass in 10- and 100-kW pilots – Analysis of conversion and lifetime using a sintered manganese ore, *Fuel* 231 (2018) 73–84, <https://doi.org/10.1016/j.fuel.2018.05.071>.
- [15] A.A. Khan, W. de Jong, P.J. Jansens, H. Spliethoff, Biomass combustion in fluidized bed boilers: potential problems and remedies, *Fuel Process. Technol.* 90 (2009) 21–50, <https://doi.org/10.1016/j.fuproc.2008.07.012>.
- [16] L.L. Baxter, T.R. Miles, T.R. Miles, B.M. Jenkins, T. Milne, D. Dayton, et al., The behavior of inorganic material in biomass-fired power boilers: field and laboratory experiences, *Fuel Process. Technol.* 54 (1998) 47–78, [https://doi.org/10.1016/S0378-3820\(97\)00060-X](https://doi.org/10.1016/S0378-3820(97)00060-X).
- [17] U. Kleinhans, C. Wieland, F.J. Frandsen, H. Spliethoff, Ash formation and deposition in coal and biomass fired combustion systems: Progress and challenges in the field of ash particle sticking and rebound behavior, *Prog. Energy Combust. Sci.* 68 (2018) 65–168, <https://doi.org/10.1016/j.peecs.2018.02.001>.
- [18] M. Zevenhoven, P. Yrjas, M. Hupa, 4 Ash-Forming Matter and Ash-Related Problems, 2022.
- [19] M. Zevenhoven-Onderwater, M.O. Hman, B.-J. Skrifvars, R. Backman, A. Nordin, M. Hupa, Bed Agglomeration Characteristics of Wood-Derived Fuels in FBC, 2006, <https://doi.org/10.1021/ef050349d>.
- [20] I. Gogolev, C. Linderholm, D. Gall, M. Schmitz, T. Mattisson, J.B.C. Pettersson, et al., Chemical-looping combustion in a 100 kW unit using a mixture of synthetic and natural oxygen carriers – Operational results and fate of biomass fuel alkali, *Int J Greenh Gas Control* 88 (2019) 371–382, <https://doi.org/10.1016/j.ijggc.2019.06.020>.
- [21] I. Gogolev, A.H. Soleimanisalam, C. Linderholm, A. Lyngfelt, Commissioning, performance benchmarking, and investigation of alkali emissions in a 10 kWth solid fuel chemical looping combustion pilot, *Fuel* 287 (2021), 119530, <https://doi.org/10.1016/j.fuel.2020.119530>.
- [22] I. Gogolev, T. Pikkariainen, J. Kauppinen, C. Linderholm, B.M. Steenari, A. Lyngfelt, Investigation of biomass alkali release in a dual circulating fluidized bed chemical looping combustion system, *Fuel* 297 (2021), 120743, <https://doi.org/10.1016/j.fuel.2021.120743>.
- [23] M. Hupa, O. Karlström, E. Vainio, Biomass combustion technology development – it is all about chemical details, *Proc. Combust. Inst.* 36 (2017) 113–134, <https://doi.org/10.1016/J.PROCI.2016.06.152>.
- [24] M.P. Glazer, N.A. Khan, W. de Jong, H. Spliethoff, H. Schürmann, P. Monkhouse, Alkali metals in circulating fluidized bed combustion of biomass and coal: measurements and chemical equilibrium analysis, *Energy Fuel* 19 (2005) 1889–1897, <https://doi.org/10.1021/EF0500336>.
- [25] T. Valmari, T.M. Lind, E.I. Kauppinen, G. Sfiris, K. Nilsson, W. Maenhaut, Field study on ash behavior during circulating fluidized-bed combustion of biomass, in: 2. Ash Deposition and Alkali Vapor Condensation, 1999, <https://doi.org/10.1021/ef9800866>.
- [26] H. Kassman, M. Broström, M. Berg, L.E. Åmand, Measures to reduce chlorine in deposits: application in a large-scale circulating fluidized bed boiler firing biomass, *Fuel* 90 (2011) 1325–1334, <https://doi.org/10.1016/J.FUEL.2010.12.005>.
- [27] B.C. Chenevert, J.C. Kramlich, K.M. Nichols, Ash characteristics of high alkali sawdust and sanderdust biomass fuels, *Symp. Combust.* 27 (1998) 1719–1725, [https://doi.org/10.1016/S0082-0784\(98\)80012-X](https://doi.org/10.1016/S0082-0784(98)80012-X).
- [28] S.V. Vassilev, D. Baxter, L.K. Andersen, C.G. Vassileva, An overview of the chemical composition of biomass, *Fuel* 89 (2010) 913–933, <https://doi.org/10.1016/J.FUEL.2009.10.022>.
- [29] M. Obaidullah, J. De Ruyck, M. Obaidullah, S. Bram, V.K. Verma, J. De Ruyck, A review on particle emissions from small scale biomass combustion process integration and intensification view project erasmus mundus external cooperation window (EMECW), European commission view project a review on particle emissions from Small Scale Bi, *Int J Renew Energy Res M Obaidullah Al* 2 (2013).
- [30] L.S. Johansson, C. Tullin, B. Leckner, P. Sjövall, Particle emissions from biomass combustion in small combustors, *Biomass Bioenergy* 25 (2003) 435–446, [https://doi.org/10.1016/S0961-9534\(03\)00036-9](https://doi.org/10.1016/S0961-9534(03)00036-9).
- [31] T. Valmari, E.I. Kauppinen, J. Kurkela, J.K. Jokiniemi, G. Sfiris, H. Revitzer, Fly ash formation and deposition during fluidized bed combustion of willow, *J. Aerosol Sci.* 29 (1998) 445–459, [https://doi.org/10.1016/S0021-8502\(97\)10021-0](https://doi.org/10.1016/S0021-8502(97)10021-0).
- [32] D. Boström, N. Skoglund, A. Grimm, C. Boman, M. Öhman, M. Broström, et al., Ash transformation chemistry during combustion of biomass, *Energy Fuel* 26 (2012) 85–93, <https://doi.org/10.1021/ef201205b>.
- [33] H. Fatehi, Y. He, Z. Wang, Z.S. Li, X.S. Bai, M. Aldén, et al., LIBS measurements and numerical studies of potassium release during biomass gasification, *Proc. Combust. Inst.* 35 (2015) 2389–2396, <https://doi.org/10.1016/J.PROCI.2014.06.115>.
- [34] J.M. Johansen, M. Aho, K. Paakkinen, R. Taipale, H. Eggsgaard, J.G. Jakobsen, et al., Release of K, Cl, and S during combustion and co-combustion with wood of high-chlorine biomass in bench and pilot scale fuel beds, *Proc. Combust. Inst.* 34 (2013) 2363–2372, <https://doi.org/10.1016/J.PROCI.2012.07.025>.
- [35] J.N. Knudsen, P.A. Jensen, K. Dam-Johansen, Transformation and release to the gas phase of Cl, K, and S during combustion of annual biomass, *Energy Fuel* 18 (2004) 1385–1399, <https://doi.org/10.1021/ef049944q>.
- [36] P.A. Jensen, F.J. Frandsen, K. Dam-Johansen, B. Sander, Experimental Investigation of the Transformation and Release to Gas Phase of Potassium and Chlorine during Straw Pyrolysis, 2000, <https://doi.org/10.1021/ef000104v>.
- [37] H. Wiinikka, C. Grönberg, O. Öhrman, D. Boström, Influence of TiO<sub>2</sub> additive on vaporization of potassium during straw combustion, *Energy Fuel* 23 (2009) 5367–5374, <https://doi.org/10.1021/ef900544z>.
- [38] W. Cao, J. Li, L. Lin, X. Zhang, Release of potassium in association with structural evolution during biomass combustion, *Fuel* 287 (2021), 119524, <https://doi.org/10.1016/J.FUEL.2020.119524>.
- [39] S.C. van Lith, P.A. Jensen, F.J. Frandsen, P. Glarborg, Release to the gas phase of inorganic elements during wood combustion. Part 2: Influence of fuel composition, *Energy Fuel* 22 (2008) 1598–1609, <https://doi.org/10.1021/ef060613i>.
- [40] P.A. Tchhoffor, K.O. Davidsson, H. Thunman, Transformation and Release of Potassium, Chlorine, and Sulfur from Wheat Straw under Conditions Relevant to Dual Fluidized Bed Gasification, 2013, <https://doi.org/10.1021/ef401703a>.
- [41] H. Fatehi, M. Costa, X.S. Bai, Numerical study on K/S/Cl release during devolatilization of pulverized biomass at high temperature, *Proc. Combust. Inst.* 38 (2021) 3909–3917, <https://doi.org/10.1016/J.PROCI.2020.06.079>.
- [42] J.-E. Eriksson, M. Zevenhoven, P. Yrjas, A. Brink, L. Hupa, J.-E. Eriksson, et al., Corrosion of heat transfer materials by potassium-contaminated ilmenite bed particles in chemical-looping combustion of biomass, *Energies* 15 (2022) 2740, <https://doi.org/10.3390/EN15082740>.
- [43] A. Hedayati, H. Sefidari, C. Boman, N. Skoglund, N. Kienzl, M. Öhman, Ash transformation during single-pellet gasification of agricultural biomass with focus on potassium and phosphorus, *Fuel Process. Technol.* 217 (2021), 106805, <https://doi.org/10.1016/J.FUPROC.2021.106805>.
- [44] T. Lind, T. Valmari, E. Kauppinen, K. Nilsson, G. Sfiris, W. Maenhaut, ASH formation mechanisms during combustion of wood in circulating fluidized beds, *Proc. Combust. Inst.* 28 (2000) 2287–2295, [https://doi.org/10.1016/S0082-0784\(00\)80639-6](https://doi.org/10.1016/S0082-0784(00)80639-6).
- [45] K.O. Davidsson, J.G. Korsgren, J.B.C. Pettersson, U. Jäglid, The effects of fuel washing techniques on alkali release from biomass, *Fuel* 81 (2002) 137–142, [https://doi.org/10.1016/S0016-2361\(01\)00132-6](https://doi.org/10.1016/S0016-2361(01)00132-6).
- [46] J. Werkelin, B.J. Skrifvars, M. Zevenhoven, B. Holmbom, M. Hupa, Chemical forms of ash-forming elements in woody biomass fuels, *Fuel* 89 (2010) 481–493, <https://doi.org/10.1016/J.FUEL.2009.09.005>.

- [47] S.V. Vassilev, D. Baxter, L.K. Andersen, C.G. Vassileva, T.J. Morgan, An overview of the organic and inorganic phase composition of biomass, *Fuel* 94 (2012) 1–33, <https://doi.org/10.1016/j.fuel.2011.09.030>.
- [48] H.M. Westberg, M. Byström, B. Leckner, Distribution of Potassium, Chlorine, and Sulfur between Solid and Vapor Phases during Combustion of Wood Chips and Coal, 2003, <https://doi.org/10.1021/ef020060l>.
- [49] J.M. Jones, L.I. Darvell, T.G. Bridgeman, M. Pourkashanian, A. Williams, An investigation of the thermal and catalytic behaviour of potassium in biomass combustion, *Proc. Combust. Inst.* 31 (2007) 1955–1963, <https://doi.org/10.1016/J.PROCI.2006.07.093>.
- [50] D. Porbatzki, M. Stemmler, M. Müller, Release of inorganic trace elements during gasification of wood, straw, and miscanthus, *Biomass Bioenergy* 35 (2011) S79–S86, <https://doi.org/10.1016/j.biombioe.2011.04.001>.
- [51] D.C. Dayton, R.J. French, T.A. Milne, Direct Observation of Alkali Vapor Release during Biomass Combustion and Gasification. 1. Application of Molecular Beam/Mass Spectrometry to Switchgrass Combustion vol. 9, 1995.
- [52] J.M. Johansen, J.G. Jakobsen, F.J. Frandsen, P. Glarborg, Release of K, Cl, and S during pyrolysis and combustion of high-chlorine biomass, *Energy Fuel* 25 (2011) 4961–4971, <https://doi.org/10.1021/ef201098n>.
- [53] Z.H. Zhang, Q. Song, Q. Yao, R.M. Yang, Influence of the atmosphere on the transformation of alkali and alkaline earth metallic species during rice straw thermal conversion, *Energy Fuel* 26 (2012) 1892–1899, <https://doi.org/10.1021/EF2011645>.
- [54] H.B. Zhao, W.T. Xu, Q. Song, J.K. Zhuo, Q. Yao, Effect of steam and SiO<sub>2</sub> on the release and transformation of K<sub>2</sub>CO<sub>3</sub> and KCl during biomass thermal conversion, *Energy Fuel* 32 (2018) 9633–9639, <https://doi.org/10.1021/ACS.ENERGYFUELS.8B02269>.
- [55] J.G. Olsson, U. Jäglid, J.B.C. Pettersson, P. Hald, Alkali metal emission during pyrolysis of biomass, *Energy Fuel* 11 (1997) 779–784, <https://doi.org/10.1021/ef960096b>.
- [56] D. Nutalapati, R. Gupta, B. Moghtaderi, T.F. Wall, Assessing slagging and fouling during biomass combustion: a thermodynamic approach allowing for alkali/ash reactions, *Fuel Process. Technol.* 88 (2007) 1044–1052, <https://doi.org/10.1016/J.FUPROC.2007.06.022>.
- [57] A. Strandberg, N. Skoglund, M. Thyrel, A. Lestander, M. Brostro, R. Backman, Time-Resolved Study of Silicate Slag Formation During Combustion of Wheat Straw Pellets, 2019, <https://doi.org/10.1021/acs.energyfuels.8b04294>.
- [58] J. Fagerström, E. Steinvall, D. Boström, C. Boman, Alkali transformation during single pellet combustion of soft wood and wheat straw, *Fuel Process. Technol.* 143 (2016) 204–212, <https://doi.org/10.1016/J.FUPROC.2015.11.016>.
- [59] I. Gogolev, C. Linderholm, D. Gall, M. Schmitz, T. Mattisson, J.B.C. Pettersson, et al., Chemical-looping combustion in a 100 kW unit using a mixture of synthetic and natural oxygen carriers – Operational results and fate of biomass fuel alkali, *Int J Greenh Gas Control* 88 (2019), <https://doi.org/10.1016/j.ijggc.2019.06.020>.
- [60] C. Linderholm, M. Schmitz, M. Biermann, M. Hanning, A. Lyngfelt, Chemical-looping combustion of solid fuel in a 100 kW unit using sintered manganese ore as oxygen carrier, *Int J Greenh Gas Control* 65 (2017) 170–181, <https://doi.org/10.1016/j.ijggc.2017.07.017>.
- [61] M. Schmitz, C. Linderholm, A. Lyngfelt, Operational experience of CO<sub>2</sub> capture using chemical-looping combustion of biomass-based fuels in a 100 kW unit, *Proc. 1st Int. Conf. Negat. CO<sub>2</sub> Emiss.*, Göteborg, Sweden (2018) 1–13.
- [62] I. Gogolev, C. Linderholm, D. Gall, M. Schmitz, T. Mattisson, J.B.C. Pettersson, et al., Chemical-looping combustion in a 100 kW unit using a mixture of synthetic and natural oxygen carriers – Operational results and fate of biomass fuel alkali, *Int J Greenh Gas Control* 88 (2019) 371–382, <https://doi.org/10.1016/j.ijggc.2019.06.020>.
- [63] J.R. Jensen, L.B. Nielsen, C. Schultz-Møler, S. Wedel, H. Livbjerg, The Nucleation of Aerosols in Flue Gases with a High Content of Alkali - a Laboratory Study 33, 2010, pp. 490–509, <https://doi.org/10.1080/02786820050195340>.
- [64] Kent O. Davidsson, Klas Engvall, Magnus Hagström, John G. Korsgren, Benny Lönn, Pettersson JBC, A surface ionization instrument for on-line measurements of alkali metal components in combustion: instrument description and applications, *Energy Fuel* 16 (2002) 1369–1377, <https://doi.org/10.1021/EF020020H>.
- [65] D. Gall, J. Viljanen, I. Gogolev, T. Allgürén, K. Andersson, Alkali monitoring of industrial process gas by surface ionization—calibration, assessment, and comparison to in situ laser diagnostics, *Energy Fuel* 35 (2021) 20160–20171, <https://doi.org/10.1021/ACS.ENERGYFUELS.1C03205>.
- [66] D. Gall, M. Pushp, K.O. Davidsson, J.B.C. Pettersson, Online measurements of Alkali and heavy tar components in biomass gasification, *Energy Fuel* 31 (2017) 8152–8161, <https://doi.org/10.1021/acs.energyfuels.7b00474>.
- [67] M. Wellinger, S. Biollaz, J. Wochele, C. Ludwig, Sampling and online analysis of alkalis in thermal process gases with a novel surface ionization detector, *Energy Fuel* 25 (2011) 4163–4171, <https://doi.org/10.1021/ef200811q>.
- [68] I. Gogolev, A.H. Soleimanisalam, D. Mei, A. Lyngfelt, Effects of temperature, operation mode, and steam concentration on alkali release in chemical looping conversion of biomass—experimental investigation in a 10 kWth pilot, *Energy Fuel* (2022), [acs.energyfuels.1c04353](https://doi.org/10.1021/ACS.ENERGYFUELS.1C04353), <https://doi.org/10.1021/ACS.ENERGYFUELS.1C04353>.
- [69] U. Jäglid, J.G. Olsson, J.B.C. Pettersson, Detection of sodium and potassium salt particles using surface ionization at atmospheric pressure, *J. Aerosol Sci.* 27 (1996) 967–977, [https://doi.org/10.1016/0021-8502\(96\)00025-0](https://doi.org/10.1016/0021-8502(96)00025-0).